Vertical Piezoelectric Structures for in-plane Actuation in MEMS Sensors

Elmeri Österlund

School of Electrical Engineering

Thesis submitted for examination for the degree of Master of Science in Technology.

Espoo 23.11.2015

Thesis supervisor:

Prof. Mervi Paulasto-Kröckel

Thesis advisor:

D.Sc. (Tech.) Altti Torkkeli

Aalto University
School of Electrical
Engineering

AALTO UNIVERSITY
SCHOOL OF ELECTRICAL ENGINEERING

ABSTRACT OF THE
MASTER'S THESIS

Author: Elmeri Österlund

Title: Vertical Piezoelectric Structures for in-plane Actuation in MEMS Sensors

Date: 23.11.2015 Language: English Number of pages: 8+67

Department of Electrical Engineering and Automation

Professorship: Electronics Integration and Reliability Code: S-113

Supervisor: Prof. Mervi Paulasto-Kröckel

Advisor: D.Sc. (Tech.) Altti Torkkeli

The purpose of this Master's Thesis is to investigate the feasibility of in-plane piezoelectric actuation and to identify suitable materials and methods. The focus is on the selection of piezoelectric material and its growth method. The theory of piezoelectricity is presented and piezoelectric actuation and sensing are discussed along with piezoelectric materials. In addition, crystal growth and different growth methods are presented. MEMS gyroscopes are discussed as well.

Piezoelectricity is the electrical response that results from mechanical stress. Piezoelectric materials are used in actuation and sensing in MEMS and in other devices. Piezoelectric actuation offers advantages over other methods, including enhanced performance and lower power use.

This thesis presents an in-plane actuator with vertical sidewall structure that is more effective than other methods. This technology can be used for example in gyroscopes and other MEMS devices.

AlN is selected as the material due to its advantages over other materials, such as compatibility and availability. AlN is required to grow on vertical sidewalls and have adequate crystal quality. Out of the considered growth methods MOVPE is the only one that can meet these requirements.

Experiments show that the presented sidewall actuator structure works in in-plane actuation and has increased performance compared to current methods. The developed MOVPE process is suitable for AlN growth considering the crystal quality.

Keywords: Piezoelectric actuation, Microelectromechanical systems, Aluminium nitride, Metal organic vapour phase epitaxy, MEMS, AlN, MOVPE

AALTO-YLIOPISTO
SÄHKÖTEKNIIKAN KORKEAKOULU

DIPLOMITYÖN
TIIVISTELMÄ

Tekijä: Elmeri Österlund

Työn nimi: Vertikaaliset pietsosähköiset rakenteet aktuaatioon MEMS sensoreissa

Päivämäärä: 23.11.2015 Kieli: Englanti Sivumäärä: 8+67

Sähkötekniikan ja automaation laitos

Professuuri: Elektroniikan integrointi ja luotettavuus Koodi: S-113

Työn valvoja: Prof. Mervi Paulasto-Kröckel

Työn ohjaaja: TkT Altti Torkkeli

Tämän diplomityön tarkoitus on tutkia tasossa tapahtuvan pietsosähköisen aktuaation toimivuutta ja löytää siihen soveltuvia materiaaleja ja menetelmiä. Pääasiana on pietsosähköisen materiaalin ja sen kasvatusmenetelmän valinta. Pietsosähköisyyden teoria esitetään ja lisäksi käsitellään tarkemmin pietsosähköistä aktuaatioita ja havainnointia sekä materiaaleja. Lisäksi kiteen kasvu ja eri kasvatusmenetelmiä esitellään. Myös MEMS gyroskooppeja käsitellään.

Pietsosähköinen ilmiö on sähköinen vaste joka syntyy mekaanisesta jännityksestä. MEMS sekä muissa laitteissa käytetään pietsosähköisiä materiaaleja aktuaatioissa ja havainnoinnissa. Pietsosähköisellä aktuaatiolla on lukuisia hyötyjä verrattuna muihin menetelmiin, mm. parempi suorituskyky ja pienempi virrankulutus.

Tässä työssä esitetään tasossa toimiva vertikaaliseen rakenteeseen perustuva sivuseinä aktuaattori. Esitetty rakenne on tehokkaampi kuin muut vastaavat menetelmät. Tätä teknologiaa voidaan hyödyntää mm. gyroskoopeissa sekä muissa MEMS sensoreissa.

Materiaaliksi valitaan AlN, sillä se on soveltuvin käsitellyistä materiaaleista. AlN:n tulee kasvaa pystysuorille sivuseinille riittävällä kidelaadulla. Harkituista kasvatusmenetelmistä MOVPE on ainut joka täyttää nämä vaatimukset.

Kokeet osoittavat, että esitelty sivuseinärakenne on toimiva tasossa tapahtuvassa aktuaatiossa. Lisäksi sillä on parempi suorituskyky verrattuna tämänhetkisiin menetelmiin. Kehitetty MOVPE kasvatusprosessi on soveltuva AlN:n kasvatukseen kidelaadun kannalta.

Avainsanat: Pietsosähköinen aktuaatio, Mikroelektromekaaninen systeemi, Alumiininitridi, Metalliorgaaninen höyryfaasi epitaksia, MEMS, AlN, MOVPE

Preface

I would like to thank Professor Mervi Paulasto-Kröckel for the opportunity to work in the Electronics Integration and Reliability group and for her supervision of this thesis. I would also like to thank Doctor Altti Torkkeli for the interesting and challenging thesis topic and for his advice.

In addition, thanks to Doctor Sami Suihkonen and to M.Sc. Lauri Riuttanen. Without their help with XRD and MOVPE this thesis would have been impossible. I also want to thank all of my co-workers from EIR.

For their support, I would like to thank my friends and family. Especially I want to thank Jane for her continued support and help in writing this thesis.

Espoo, 18.11.2015

Elmeri H. J. Österlund

Contents

Symbols and Abbreviations

Symbols

A	Surface area
a, c	Lattice constants
c	Elastic modulus
D	Electric displacement
d	Piezoelectric coefficient (C/N)
d	Lattice plane spacing
E	Electric field
e	Piezoelectric coefficient (C/m^2)
F_{piezo}	Piezoelectric force equal
f_i	Lattice misfit
$\mathbf{g}$	Reciprocal lattice vector
$\mathbf{G}$	Reciprocal lattice point vector
i_{ac}	Current
i_{mot}	Motional current
P	Electrical polarization
p	Pressure
Q	Gas flow
q	Elemental charge
R	Electron range
S	Mechanical strain
$\mathbf{S}$	Scattering vector
T	Mechanical stress
t_c	Critical thickness for heteroepitaxial films
v	Actuation voltage
hkl	Miller's indices, X-ray reflection
(hkl)	Crystal plane
$\{hkl\}$	Family of crystal planes
$[hkl]$	Direction in a crystal
$< hkl >$	Family of directions
Δx	Resolution
ε	Dielectric permittivity
ϵ	Misfit strain
η	Transduction factor
λ	Wavelength
ν	Poisson's ratio
Ω	Angular velocity
ω	Angular frequency
ω	Angle between incident beam and sample surface
ρ	Resistivity
ρ	Density
θ	Angle between incident beam and lattice planes

Abbreviations

ALE	Atomic layer epitaxy
AlN	Aluminium nitride
CG	Columnar growth
CMOS	Complimentary metal oxide semiconductor
CTE	Coefficient of thermal expansion
CVD	Chemical vapour deposition
DC	Direct current
EDS	Energy-dispersive X-ray spectroscopy
FBAR	Thin film bulk acoustic resonator
FEM	Finite element method
FM	Frank-van der Merwe
FWHM	Full width at half maximum
HEMT	High electron mobility transistor
IC	Integrated circuit
KOH	Potassium hydroxide
LED	Light emitting diode
MBE	Molecular beam epitaxy
MEMS	Microelectromechanical system
MOVPE	Metal organic vapour phase epitaxy
NH_3	Ammonia
PLD	Pulsed laser deposition
PVD	Physical vapour deposition
PZT	Lead zirconate titanate
RF	Radio frequency
RIE	Reactive ion etching
RoHS	Restriction of Hazardous Substances Directive
SEI	Secondary electron imaging
SEM	Scanning electron microscopy
SF	Step-flow
SiO_2	Silicon dioxide
SK	Stranski-Krastanov
SOI	Silicon-on-insulator
TMAl	Trimethylaluminium
UV	Ultraviolet
VW	Volmer-Weber
XRD	X-ray diffraction
ZnO	Zinc oxide
ZnS	Zinc sulphide
Å	Ångström, 0.1 nm

1 Introduction

Piezoelectric microelectromechanical systems (MEMS) are a currently emerging technology. In actuation, compared to electrostatic methods, piezoelectric materials offer such advantages as higher electromechanical coupling and lower power consumption. Moreover, piezoelectric materials can be used in sensing as well. Utilization of the piezoelectric effect also opens up energy harvesting possibilities. Piezoelectric structures are also relatively easy to implement compared to other methods. Recently, piezoelectric actuation has been adopted in gyroscopes, where orthogonal vibration modes are required in order to sense angular momentums. Piezoelectric materials have also been used in thin film bulk acoustic resonators (FBAR). Though this technology has been developed mainly independent of the MEMS field. [1, 2]

Piezoelectric actuators operate by expanding or contracting in response to an applied electric field. Strain of the piezoelectric material is used to deform the rest of the actuator structure and create displacements. In addition to the piezoelectric material, electrodes are required for the application of the electric field. The electrodes and the piezoelectric material are typically on top of a substrate, which acts as a beam that bends and provides mechanical support. [1]

There are certain challenges in piezoelectric actuation due to limitations in current micromachining methods. Actuators working out-of-plane (Figure 1a) are relatively simple to fabricate using surface micromachining. In-plane movement can also be excited using a small change to the previous configuration. Two piezoelectric strips (split electrode) expand and contract anti-phase. However, this may induce unwanted twisting motion in the actuator beam, as shown in Figure 1b. Moreover, the placing of the piezoelectric elements is not optimal.

The solution to the aforementioned problem is to actuate using the vertical sidewalls of the beam, as shown in Figure 1c. This configuration also enables larger electrodes, which further enhances the performance of the actuator [1]. Moreover, the electrode placement is more efficient in generating displacement in this configuration.

Currently, no established fabrication methods exist for the vertical sidewall structure. The purpose of this Master's Thesis is to investigate the feasibility of piezoelectric sidewall actuation. This consists of finding suitable materials and growth methods. In addition, preliminary experimental studies are conducted in order to test the selected material and growth method. This thesis is divided into two parts: theoretical and experimental.

The theoretical part of this thesis begins with theory of piezoelectricity in Section 2. In addition, different piezoelectric materials are presented and piezoelectric actuation and sensing is explained. Crystal growth is discussed in Section 3. This section aims to present the requirements for crystal growth. Different growth methods are presented in Section 4, with evaluation about their suitability for this work. The planned device is presented in more detail in Section 5. The operating principle of a gyroscope is presented. In addition, the selection of electrode material and fabrication of the structure is discussed. Finally, different characterization methods used are presented in Section 6.

The experimental part begins by presenting the sample fabrication and planned

experiments in Section 7. Results of the fabrication and results of the characterization are presented and discussed in 8. Finally, a conclusion of the work done in this Master's Thesis is given in section 9.

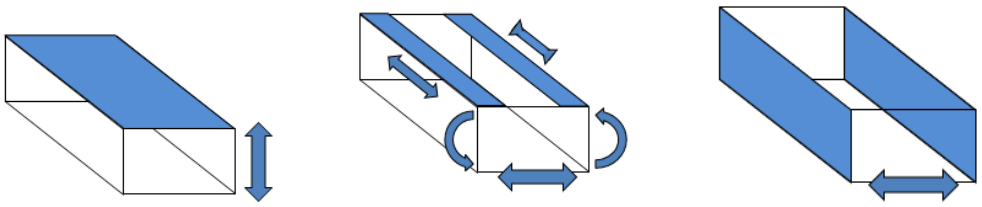

(a) Out-of-plane actuation configuration.

(b) In-plane actuation using split electrode excitation from the top.

(c) In-plane actuation from the vertical sidewalls.

Figure 1: Different actuation configurations for beam actuator. Actuator material placement in blue.

2 Piezoelectricity

In short, piezoelectricity is the linear coupling between mechanical stress and electric field in piezoelectric materials [3]. In this section, the theory of piezoelectricity is presented. Piezoelectric actuation and sensing is presented and discussed later in Section 2.1. Piezoelectric materials are presented in Section 2.2 after that.

Two kind of piezoelectric effects exist: the direct and the converse effect. Direct piezoelectric effect linearly couples mechanical stress to electric polarization, whereas converse effect couples mechanical strain to applied electric field. The piezoelectric coefficient d relates the coupled quantities together according to Equations (1a) and (1b) for direct and converse piezoelectric effect, respectively.

$$P = dT, \tag{1a}$$

$$S = dE, \tag{1b}$$

where P is the electrical polarization, T is the mechanical stress, S is mechanical strain and E is the applied electrical field. The units of the piezoelectric coefficient are coulomb per newton (C/N) and metre per volt (m/V), for direct and converse effect, respectively. However, the units are equivalent with each other and the former is typically used. Typical useful coefficients range from 1 to 1 000 pC/N. [3]

As all the quantities involved here are dimensional, so is the piezoelectric coefficient. In fact, a total of 27 individual coefficients are required to fully describe the piezoelectric behaviour. However, only 18 can be independent due to the symmetry of mechanical stress, and in practice significantly fewer are needed. The equations (1a) and (1b) can be written in either tensor or matrix notation. In this thesis the matrix notation is preferred. It uses a 6×3 matrix to describe the piezoelectric coefficients. For the direct effect the full equation is

$$\begin{pmatrix} P_1 \\ P_2 \\ P_3 \end{pmatrix} = \begin{pmatrix} d_{11} & d_{12} & d_{13} & d_{14} & d_{15} & d_{16} \\ d_{21} & d_{22} & d_{23} & d_{24} & d_{25} & d_{26} \\ d_{31} & d_{32} & d_{33} & d_{34} & d_{35} & d_{36} \end{pmatrix} \begin{pmatrix} T_1 \\ T_2 \\ T_3 \\ T_4 \\ T_5 \\ T_6 \end{pmatrix}, \tag{2}$$

where 1, 2, and 3 indicate three orthogonal directions, T_1, T_2 and T_3 uniaxial stresses and T_4, T_5 and T_6 shear stresses. [3] In piezoelectric literature sub-indices 1, 2 and 3 are used instead of x, y and z to note different directions. The convention is to orient the coordinate axes so that the 3-direction is along the polar axis of the piezoelectric material. Typically, the piezoelectric effect in materials is strongest in this direction [2, 3]. The same convention for noting the directions is used in this thesis.

The converse piezoelectric coefficient matrix is the transpose of the direct coefficient matrix. Equation (1b) in matrix form is then

$$\left(S\right) = \left(d\right)^t \left(E\right), \tag{3}$$

where $()^t$ is the matrix transpose. [3]

From practical point of view Equations (1a) and (1b) may not be the most useful ones. Equations that account for the full state of stress and electric displacement of the material are respectively

$$T = cS - eE, \tag{4a}$$
$$D = \varepsilon E + eS, \tag{4b}$$

where c is elastic modulus, e is the piezoelectric coefficient, ε dielectric permittivity and D is the electric displacement [1]. In Equations (4a) and (4b) the piezoelectric coefficient is marked with e instead of d in order to differentiate it from the constant used in (1a) and (1b). The relation between d and e is $e = cd$, and e is expressed in $\mathrm{C/m^2}$. The directions for the coefficient and elastic modulus need to obviously match. As strain and stress are inherently linked through the elastic compliance coefficients and vice versa with stiffness coefficients, equations (1a) and (1b) can be rewritten using strain in place of stress ($P = eS$) and vice versa ($T = -eE$). [2]

The majority of piezoelectric devices fall under two categories: longitudinal and transverse. This simplifies the treatment of the equations greatly. In the longitudinal configuration the piezoelectric coefficient e_{33} couples strain S_3 and electric displacement D_3 together. All other strains and electric fields are zero. In the transverse configuration, strain is perpendicular to the electric field. The piezoelectric coefficient e_{31} couples the orthogonal electric displacement D_3 to strain S_1. All other strains and electric fields are zero.

In actual use however, the piezoelectric thin film is typically used as a part of a composite structure. Other parts can be for example metallic electrodes and a silicon cantilever. In this case, the elastic behaviour of the device is mainly dominated by the silicon beam. In reality, no deformation mode is defined by a single piezoelectric coefficient. Analytical analysis of such devices is not easy unless some special conditions exist and assumptions are made. In practice, finite element method (FEM) simulations are required for accurate understanding of device operation. [2] Simplified piezoelectric actuation and sensing will be considered next in Section 2.1.

2.1 Piezoelectric Actuation and Sensing

Piezoelectric actuation relies on the fact that piezoelectric materials deform under electric field. As the planned device in this thesis works in the transverse configuration, only transverse actuation will be discussed here.

Piezoelectric actuation and sensing offers many advantages over electrostatic, thermal and magnetic methods. The main advantage is the higher electromechanical coupling. Piezoelectric methods also enable relatively easy implementation of resonant structures. Whereas electrostatic actuation requires small features, mainly for the electrode gap. This in turn requires accurate patterning and processes. Moreover, piezoelectric devices are more stable. With regards to power use, piezoelectric sensors itself do not require additional power. Actuation uses less power than other methods as well. Moreover, energy harvesting from mechanical noise becomes possible if the actuator or sensor is not constantly in use. In addition, signal handling for actuation and sensing is relatively easy. [1, 2]

For large actuation amplitudes, electrostatic actuation requires high voltages. There is also a threshold voltage, where the electrodes snap into contact with each other (snap-in voltage). Also, electrostatic actuation can only pull electrodes together, not push them away regardless of the sign of the voltage. Thermal and magnetic methods typically require high power. Moreover, thermal methods can be inherently slow due to heating up times. In contrast, piezoelectric devices can achieve large amplitude actuation with low drive voltages almost instantly. [1, 2]

In the selected configuration the strain is perpendicular to the electric field as shown in Figure 2. The coefficient e_{31} couples the orthogonal electric displacement D_3 and strain S_1 together. Other strains and electric fields are assumed to be zero. This assumption causes some error, however it is small. [1]

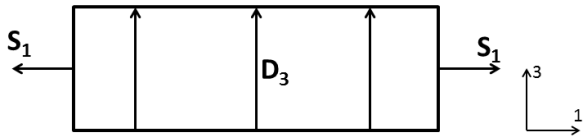

Figure 2: Transverse piezoelectric actuator configuration. Adapted from [1].

With directions taken into account, Equation (4a) becomes

$$T_1 = c_{11}S_1 - e_{31}E_3, \tag{5}$$

and if free deformation of the material is assumed the total stress will be zero and the strain is

$$S_1 = \frac{e_{31}}{c_{11}}E_3 = \frac{e_{31}}{c_{11}t}v, \tag{6}$$

where t is the thickness of the piezoelectric layer and v the voltage applied over the layer. In case of uniform strain ($S_1 = \Delta L/L$), the length extension ΔL of the actuator is

$$\Delta L = \frac{e_{31}L}{c_{11}t}v, \tag{7}$$

where L is the length of the actuator. As can be seen from the previous equation, the actuator dimensions affect the actuator displacement. Maximising the $\frac{L}{t}$-ratio yields the largest stroke. [1]

The piezoelectric effect can also be thought as a force acting on the ends of the actuator. The force equal is

$$F_{piezo} = \frac{e_{31}A_1}{t}v, \tag{8}$$

where A_1 is the end cross sectional surface area of the actuator. [1] From this equation it follows that the force produced by this type of actuator does not depend on the thickness of the piezoelectric material. This is because the end cross sectional area is $A_1 = th$, where h is the width of the material. Thus, the thickness terms cancel each other out in Equation (8) and the equation becomes

$$F_{piezo} = e_{31}hv. \tag{9}$$

One important figure of merit in electromechanical actuation is the transduction factor η. It defines how the drive voltage relates to actuation force as

$$F = \eta v, \tag{10}$$

where F is the force generated by the actuator and v is the drive voltage. From Equation (8) the ideal transduction factor is simply $\frac{e_{31}A_1}{t}$. However, there are factors that reduce the actual achieved factor. One major factor that can reduce the transduction factor is the electrode placement. [1]

Effectively, the actuator structure is a resonator when actuated at its resonant frequency for maximum vibrational amplitude. For this reason it can be modelled as such. As a result of the vibration mode shape the resonator will have an effective mass and elasticity that are different from the actual values. The mode shape is needed in calculating the effective mass, spring constant and resonant frequency.

When the actuator is driven with an alternating voltage a current will run through it. This current can be divided into two parts, the AC part i_{ac} and so called motional current i_{mot}. The AC part is simply the current running through the capacitor structure formed by the two electrodes and the piezoelectric material, which acts as the capacitor dielectric. The motional current is caused by the second term on the left side of Equation (4b). Integration of the previous equation over the actuator dimensions gives the total current as

$$i = sC_0v + se_{31}AS_1 \equiv i_{ac} + i_{mot}, \tag{11}$$

where C_0 is the capacitance and $s = j\omega$ (j is the imaginary unit and ω is the angular frequency $2\pi f$). In the equation for the current it is assumed that the strain in the actuator is uniform. In other cases actual displacements at the actuator edges need to be used. [1]

In the previous discussion, it was assumed that the actuator consisted only of the piezoelectric material. Moreover, the material was free to deform. In actual use this will not be the case, and the piezoelectric material will be a part of a larger structure. The deformation of the material is thus limited. Moreover, the goal is bending of the structure, not extension. Because of this, the structure will be in complex stress state and analytical consideration of the structure is difficult. For this reason, the structure is simulated in Section 5.

Due to the dual nature of piezoelectricity, the same device can be used in sensing as well. In this case, the deformation of the structure will generate and electric field, which is then measured. Piezoelectric sensing is already used in applications such as microphones, accelerometers and record player pickups. In sensing, the piezoelectric element creates an electric current that is proportional to the rate of changing strain according to Equation (11). [1] Whereas in actuation the important figure of merit was simply the transverse coefficient e_{31}, in sensing the figure of merit for a material is e_{31}/ε_{33}. In other words, material with small dielectric permittivity is suitable for sensor applications. [2]

2.2 Piezoelectric Materials

Different piezoelectric materials are presented and compared in more detail here. The important material properties for this work are discussed as well. Based on the discussion, selection of piezoelectric material is done.

In order for a material to exhibit piezoelectric properties, the moving atoms in its crystal structure need to cause polarization under deformation. All piezoelectric coefficients are zero in all centric crystals and untextured polycrystalline materials. In centric crystals no polarization occurs and in untextured materials randomly oriented grains cancel each other out. [3]

Most piezoelectric materials, with the notable exception of quartz, have a polar axis. It is common to assign the 3-axis along it, in the direction that results in a positive d_{33} coefficient. As thin films are single crystalline only in special cases, most being polycrystalline, the effect of crystal structure on piezoelectricity needs to be considered. The piezoelectric effect is the average of all the grains. What this means in practice is different for ferroelectric and non-ferroelectric materials. Reorientation of the polar axis is possible for the former, thus original orientation of the grains is not as import as for non-ferroelectric materials. [2]

For non-ferroelectric materials on the other hand, the material growth needs to result in a textured film. This means that the polar axes of different grains need to be aligned in the same direction. Further discussion on film growth can be found in Section 3. Moreover, the polar axis should be aligned perpendicular to the film surface for two reasons. First, the piezoelectric effect is typically strongest in this direction. In many cases it is the only direction in which materials have an response to electric field. Second, it makes the most sense to use a parallel plate capacitor configuration in applying the electric field over the material. In this way, applying the voltage over the thinnest part highest field strength can be achieved and common micromachining methods can be used. [2, 3]

The requirements on film growth results are more relaxed for ferroelectric materials. As previously mentioned, the polar axis in them can be reoriented. This is called pooling and is done using a high electric field, typically at elevated temperature. The common notation is again to assign the 3-direction to be out-of-plane. Thus, the remaining 1 and 2 directions are in-plane. Moreover, they are equivalent for poled and polycrystalline films, thus $d_{31} = d_{32}$. For single crystalline materials, they are equivalent only if the polar axis is centre of threefold or higher rotational symmetry. [2]

11 of the 32 crystal classes and 4 of the 7 Curie groups are not piezoelectric. A center of symmetry in the crystal structure eliminates all piezoelectric coefficients. Crystals with tetrahedral groups are often piezoelectric, for example zinc oxide (ZnO), zinc sulphide (ZnS) and quartz (SiO_2). As previously mentioned, there can be 18 independent piezoelectric coefficients. In practice, most piezoelectric materials have less than that due to symmetry elements in them. [3]

Neumann's law states that any physical properties of a material must have the same symmetry as the crystal structure of the material. In practice this means that the piezoelectric matrix for a material must remain the same after symmetry

transformations. Different symmetry elements, such as mirror planes and rotation axes, require that many of the piezoelectric coefficients are zero. [3]

Commonly used piezoelectric materials include for example quartz, lead zirconate titanate (PZT) and aluminium nitride (AlN). The piezoelectric coefficients depend on direction of stress (or strain) and electric field (or polarization). Coefficients for different materials are presented in Table 1. [3] The properties of PZT vary over a wide range depending on the exact composition of the material, orientation of the polar axis and poling.

Table 1: Some common piezoelectric materials and their piezoelectric coefficients.

Material	d (pC/N) [3]	e (C/m^2) [1]	ε_{33}
AlN	$d_{33} = 5.0$	$e_{33} = 1.55$	10.4 [4]
	$d_{31} = -2.0$	$e_{31} = -1.02$ [4]	
ZnO	$d_{33} = 12.4$ [5]	$e_{33} = 1.14$	10.9 [5]
	$d_{31} = -5.0$ [5]	$e_{31} = -0.61$	
PZT	$d_{33} = 593$	$e_{33} = 15.1 \cdots 15.8$	
	$d_{31} = -274$	$e_{31} = -4.3 \cdots -7.7$ [1, 6]	$1300 \cdots 1500$ [1]
	$d_{15} = 741$		
Quartz	$d_{11} = 2.3$	$e_{11} = 0.171$ [7]	4.62 [7]
	$d_{14} = -0.67$	$e_{14} = -0.04$ [7]	

Requirements for the material are high piezoelectric constant, compatibility with silicon and micromachining processes, availability and existing deposition methods. Small dielectric constant and high dielectric strength would be advantageous as well. Moreover, the deposition method should provide adequate step coverage for the sidewall deposition. Deposition requirements will be further discussed in Section 4.

Out of the materials listed above, PZT clearly has the strongest piezoelectric effect. However, deposition methods for PZT are somewhat limited, which will be discussed later in more detail. Moreover, because PZT contains a high amount of lead, its use in the future may become limited. Although currently PZT is exempt from the RoHS regulations. [8]

Quartz is another very popular material. This is mainly because if cut in a certain way, it has a very high temperature stability. This is especially important in resonator applications that require a stable frequency over time. For the purposes of this work quartz is not a suitable material, because it lacks the d_{31} constant needed for transverse actuation and sensing. [3]

Even though AlN has one of the smallest piezoelectric effects of the materials listed above, it is one of the most used in the semiconductor and MEMS industry. It has a high electrical resistivity and it is compatible with CMOS processes. A wide range of methods exist for growth of AlN. Moreover, it is already commonly used in piezoelectric and other applications. Lasers and LEDs operating in the UV and near UV spectrum utilize the wide band gap of AlN. It is also used in solar cells and high electron mobility transistors (HEMT). [9] It has also been suggested as a possible replacement for SiO_2 in silicon-on-insulator (SOI) substrates [10].

In addition to AlN, ZnO is also commonly used in MEMS applications. Both materials have a wurtzite structure with a polar axis along the [001] direction. Both are also commonly sputter deposited. Whereas AlN is compatible with current semiconductor technology, use of ZnO can be challenging due to fast diffusion of zinc atoms into silicon. The resistivity of ZnO can be a problem as well. ZnO has a smaller band gap and it is essentially a semiconductor, thus there is a risk of doping and a further decrease in resistivity. High conductivity is a problem because it leads to high dielectric losses at typical actuator and sensor operating frequencies of below 10 kHz. Moreover, ZnO needs to be grown at low temperatures for high resistivity, which typically leads to poor crystal quality and reduced piezoelectric coefficients. Effects of growth temperature are further discussed in Section 3. [2, 11]

Previously though, ZnO has been more widely used due to its better availability over AlN. However, this is no longer the case. AlN is better suited for deflecting structures, such as the one proposed in this work. This is because AlN has higher transverse piezoelectric coefficient than ZnO when in thin film form. [2]

In addition to the materials presented above, there is a wide range of ternary and quaternary piezoelectric ceramics. However, these materials are outside the scope of the thesis, as they are highly experimental. Moreover, the available growth methods for these materials are limited.

As a conclusion of the above discussion, AlN is selected as the piezoelectric material for this work, due to its compatibility, piezoelectric properties and availability.

Next, the crystal structure and piezoelectric properties of AlN are presented in more detail. The crystal structure is a hexagonal wurtzite, as shown in Figure 3 and belongs to symmetry group $6mm$, which means it has a 6-fold rotational symmetry axis and two mirror planes parallel to it. As can be seen, two of the lattice vectors are of equal length, $a_1 = a_2$ and the angle γ between them is 120°. Third lattice vector $\mathbf{a_3}$ is perpendicular to both vectors ($\alpha = \beta = 90°$). Commonly, $\mathbf{a_1}$ and $\mathbf{a_2}$ are named simply $\mathbf{a}$ and $\mathbf{a_3}$ is named $\mathbf{c}$. Thus, [001] oriented AlN films are commonly called c-axis oriented. The full piezoelectric coefficient matrix for AlN is

$$\big(d\big) = \begin{pmatrix} 0 & 0 & 0 & 0 & d_{15} & 0 \\ 0 & 0 & 0 & d_{15} & 0 & 0 \\ d_{31} & d_{31} & d_{33} & 0 & 0 & 0 \end{pmatrix}. \text{ [3]} \tag{12}$$

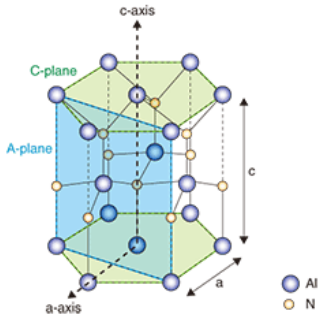

Figure 3: The hexagonal wurtzite structure of AlN. [12]

3 Crystal Growth

In this section, the principles of crystal growth are presented. The aim of this section is to identify what is required for the growth of high quality single crystalline or textured polycrystalline films. The section is further divided into separate subsections on different growth modes, nucleation of films and heteroepitaxy. Heteroepitaxy is presented in its own section since it is important regarding this work.

In general, epitaxial crystal growth refers to the growth or deposition of material on a substrate. In the strictest sense, epitaxy refers only to the growth of single crystalline layers, that have adopted the lattice constant of the substrate. In this thesis, epitaxy and growth of relaxed crystals is considered. Relaxed crystals do not have the lattice constant of the substrate. The result of crystal growth needs to be either single crystalline or polycrystalline layer of material with preferential crystal orientation (textured). [11, 13] Both types of crystal structure will be discussed in this section, since both types satisfy the requirements for piezoelectric properties.

Crystal growth is defined as heteroepitaxy if there is at least one parameter that differs between the growing layer and the substrate. The parameter can be for example the lattice constant or the chemical structure. When the growing material is the same as the substrate, the term homoepitaxy is used. In heteroepitaxy the crystallographic orientation of the growing film cannot be generally predicted. Moreover, no *a priori* solutions exist to how certain orientations can be selected by choosing suitable growth conditions. [11, 13]

The growth process can be considered as a phase transition between two phases. The first phase is metastable and the second one is stable. The metastable phase contains the precursors from which the stable phase grows. In reality the process is more complex and many phases exist during the growth. The stable phase consists of the grown material and possible impurities. The exact composition and details of the metastable phase depend on the growth method and precursors used, which will be discussed in more detail in Section 4. In theory, the stable phase depends only on the deposited material. However, the growth method affects such qualities of the deposited material as impurity concentrations, crystal quality and defects. The selected substrate affects the properties of the stable phase at the early stages of growth as well. [11]

In order for crystal growth to occur at all, there needs to be a driving force for the phase transition. This is generated by the supersaturation of the metastable phase. As a result, mass transport occurs between the phases. However, this alone does not necessarily results in crystal growth. Crystal growth is possible if the difference between the lattice constants of the growing film and substrate is sufficiently small, typically less than 15% [11]. In equation form this lattice mismatch condition can be presented as

$$\left|\frac{a_f - a_s}{a_s}\right| < 0.15, \tag{13}$$

where a_f and a_s are the lattice constants of the growing film and the substrate, respectively. The growth of the film occurs first at the interface between the substrate and the metastable phase. After the first complete monolayer of the growing film

has formed, the growth continues at the interface between the growing film and the metastable phase. How the growth continues depends on the lattice misfit, supersaturation, growth temperature and on the adhesion between arriving atoms and substrate. [11]

Generally, the crystal growth process happens by the following mechanisms. First, small clusters of atoms nucleate on the substrate. These nuclei continue to grow and agglomerate into small islands. As the growth continues, these islands connect together forming chains and eventually covering the substrate. However, the islands do not cover the substrate completely and small holes and channels remain. Eventually, the whole surface is covered as holes and channels are filled. [11]

In addition, the microstructure of the deposited films continues to evolve during growth. Recrystallization and grain boundary migration processes continue during growth between connected islands. [11] However, the process described before is just a generalization and actual growth process can occur differently depending on growth parameters. Next, different growth modes and nucleation will be presented in more detail.

3.1 Growth Modes

The crystal can grow by five different growth modes. The substrate influences the growth at the early stages. For example, the growth is affected by the lattice misfit and thermal stress along with chemical interactions and defects at the interface. The five different growth modes are: Volmer-Weber (VW), Frank-van der Merwe (FM), Stranski-Krastanov (SK), columnar growth (CG) and step-flow (SF) mode. [11]

Which of the growth modes listed above occurs depends on factors such as lattice misfit, supersaturation of the crystallizing phase, growth temperature and adhesion energy between substrate and the growing crystals. [11]

In VW growth mode the atoms or molecules are more strongly bond to each other than to the substrate. As a result they form small clusters on the substrate. These clusters will continue to grow into separate islands. In the opposite case the deposited atoms or molecules bond to the substrate more strongly than to each other. In this case, FM growth occurs. This growth mode is also known as layer by layer growth. The deposited atoms or molecules first form a complete monolayer on the substrate. After that subsequent layer are grown on top of each other, provided that the decrease in binding strength is monotonic towards the bulk strength of the deposited material. [11]

SK mode is a combination of the two modes mentioned above (VM and FM). It is also known as layer + island growth. In this mode, after one or two monolayers layer growth is no longer favourable and islands begin to form. The formation of islands can be caused by any disruption in the monotonic decrease of the binding strength. The disruption can be caused for example by high interface energy or when the growing film is highly strained. [11]

During both of the island growth modes (VM and SK) the formed islands tend to coalesce together and cover the whole substrate as the film grows thicker. If the atomic mobility is not high enough on the substrate or on the growing film, the

islands will remain separate. In this case CG mode occurs and continuous film over the substrate is not formed. Typically, the columns formed are highly defective. [11]

The last growth mode is the SF mode. In this mode, the film is grown in a layer by layer fashion as in FM. However, in SF the growth occurs by advancement of atomic steps along terraces. This requires the existence of steps on the substrate surface, which can be guaranteed by misorientation of the wafer cut. Instead of cutting the substrate directly along crystal planes, it is cut at an angle with respect to the crystal planes. Moreover, SF mode requires sufficient mobility of the adatoms on the surface. This requires the combination of high growth temperature and sufficiently low incoming flux of atoms or molecules to the surface. [11]

In short, the difference between SF and FM modes is that in SF, the diffusion length of adatoms is larger than the terrace width. In FM the diffusion length is shorter than terrace width. The SF growth mode differs from the four other growth modes in that it requires no nucleation, as adatoms bind at terraces. [11]

3.2 Nucleation

Nucleation is the spontaneous formation of small clusters of adatoms on the substrate surface. It is an important precursor in crystal growth and in overall crystallization process. As mentioned before, nucleation is required in all growth modes, with the exception of SF growth. Clusters have more energy than in bulk due to the increased surface-to-volume ratio. Thus, supersaturation is required for cluster stability. [11]

Orientational behaviour of the growing layer can be influenced by nucleation or by subsequent growth. Thus, crystal growth can be divided into two groups: layers whose orientation is determined by the initial nuclei, and to subsequent growth controlled layers. Crystal growth can also be divided into three different categories depending on the relationship between the growing film and the substrate. In the first category (Figure 4a), the grown film is completely non-oriented with respect to the substrate and to individual grains. Second category crystals are grown with the same stable low index lattice plane (Figure 4b). However, they are not oriented with respect to each other. These kind of films are also called textured. In the last, third category crystals have textural and azimuthal orientation towards each other (Figure 4c). Category two and three films can also be referred as epitaxial films. [11]

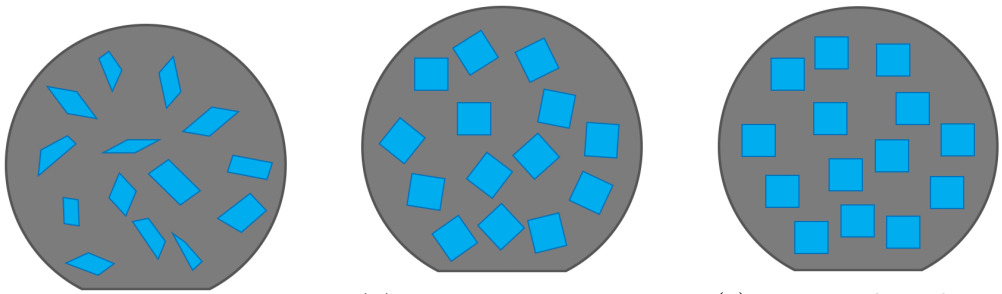

(a) Non-oriented.

(b) Textured orientation.

(c) Textural and azimuthal orientation.

Figure 4: Different orientational behaviour of the growing grains. Adapted from [11].

On the other hand, in some cases the nuclei can move and rotate on the surface. When the nuclei are able to reorient themselves before coalescence, the crystal growth becomes a post-nucleation process. The initial orientation and location of the nuclei does not influence the film orientation. [11]

3.3 Heteroepitaxy

Heteroepitaxy will be presented in more detail here, since it is an important concept in this thesis. Additionally, strain and lattice defects induced by the lattice mismatch are presented as well.

Single crystalline layers grown by heteroepitaxy can be epitaxial or not, depending on if the interface between the epilayer and substrate is crystallographically perfect or not. If the layer is not epitaxial, also called incoherent, it can have any in-plane lattice constant that minimizes the free energy of the lattice. However, if the layer is epitaxial (coherent), it will have the in-plane lattice constant of the substrate. This will lead to strain in the epilayer and this in turn can increase significantly the free energy. Coherent and incoherent film lattices are schematically presented in Figure 5. [11]

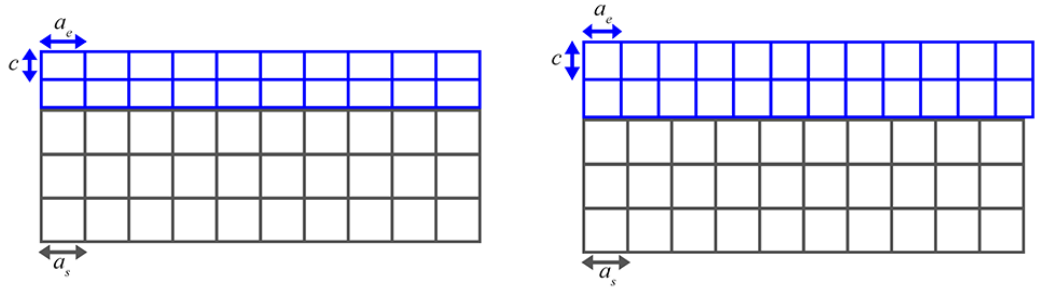

(a) Epitaxial film. The lattice constant of the film is strained to match the substrate.

(b) Incoherent or not epitaxial. The film is relaxed and can have any lattice constant that minimises the free energy.

Figure 5: Coherent epitaxial and incoherent not epitaxial films on a substrate.

There are three main factors that affect the strain of the growing layer: lattice constant matching, crystallographic orientation and surface geometry. In heteroepitaxy, the lattice constant matching is the most significant problem. The misfit f_i can be defined as

$$f_i = \frac{a_{si} - a_{ei}}{a_{ei}}, i = \{1, 2\} \tag{14}$$

where a_{si} and a_{ei} are the lattice constants of the substrate and growing film, respectively and 1 and 2 are the directions perpendicular to the growth direction (3-direction). [11] In this thesis all the involved materials have equivalent 1 and 2 directions ($f_1 = f_2$), thus it is not necessary to use the full notation.

The misfit strain ϵ is equal to the misfit f if the film is coherent with the substrate and the misfit is sufficiently small. However, when the strain energy is high enough,

it can generate dislocations that accommodate part of the misfit. In this case, the misfit is

$$f = \epsilon + d, \tag{15}$$

where d is the misfit accommodation by dislocations. For very thin films, the misfit can be defined also as

$$f = \frac{a_e - a_s}{a_s}, \tag{16}$$

instead of Equation (14). [11]

During heteroepitaxy, the first few atomic layers will be strained to match the substrate, given that the misfit is sufficiently small. This phenomenon is called pseudomorphism. When the film grows thicker, the strain energy increases until it is high enough to generate dislocations. This gives a critical thickness for heteroepitaxially grown films. [11] This thickness can be approximated as

$$t_c \approx \frac{a_e^2}{2(a_s - a_e)}, \tag{17}$$

thus, if the film is thicker than t_c it is energetically favourable for it the relax by generating dislocations [14].

If the film is not fully relaxed by dislocations, it will be strained and the lattice constants of the film will change. The strains can be defined by measuring the lattice constants, which is presented in more detail in Section 6.1. Due to the lattice mismatch in heteroepitaxy dislocations and other lattice defects as well as strain is expected in the grown film. The out of plane ϵ_c and in-plane ϵ_a strains can be defined as

$$\epsilon_c = \frac{c_{meas} - c_0}{c_0}, \tag{18}$$

and

$$\epsilon_a = \frac{a_{meas} - a_0}{a_0}, \tag{19}$$

where c_{meas} and a_{meas} are the measured and c_0 and a_0 are the unstrained reference for out of plane and in-plane lattice parameters, respectively. The strains are coupled together by distortion factor D according to

$$\epsilon_c = -D\epsilon_a = -\frac{2c_{13}}{c_{33}}\epsilon_a = \frac{2\nu}{1-\nu}\epsilon_a, \tag{20}$$

where c_{13} and c_{33} are components of the elastic stiffness and ν is the Poisson's ratio. For determining the strain the reference parameters need to be accurately known. [9]

4 Growth Methods

A wide variety of different methods exists for deposition and growth of thin films. These methods all have different characteristics and some are more suitable for specific tasks than others. In this section, different growth methods will be presented. Their suitability for deposition of AlN as well as deposition on vertical structures will be discussed. Different growth methods will be compared and the most suitable one is selected.

For this work, the growth methods needs to fulfil two main requirements. Firstly, the crystal quality of the film needs to meet the requirements for piezoelectricity, presented previously. Secondly, the film needs to grow adequately on the vertical sidewalls. Generally, the film thickness is different on horizontal and vertical surfaces, as illustrated in Figure 6. This is especially the case with sputtering, which will be presented later. High temperature chemical vapour deposition (CVD) processes have better uniformity between surfaces due to fast surface diffusion and other effects. The ratio R between the film thicknesses can be used as a general figure of merit for conformal coverage

$$R = \frac{t_v}{t_h}, \tag{21}$$

where t_v and t_h are the film thicknesses on vertical and horizontal surfaces, respectively (See Fig. 6). [13]

The quality of the film on sidewall may be different than on the top surface, even though adequate conformal coverage is achieved. Conformal coverage also depends on the aspect ratio of the structure. Moreover, the aspect ratio changes during the growth. [13] However, the effect of aspect ratio is not considered in this work because the aspect ratio of the planned structures is low and the change during growth is negligibly small.

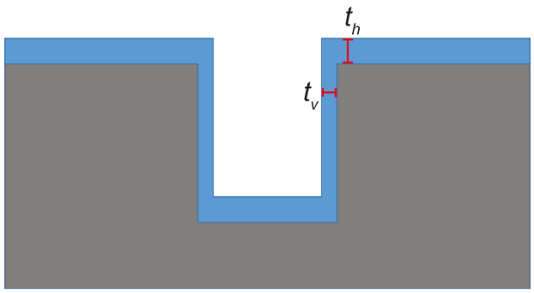

Figure 6: Difference in film thickness on horizontal and vertical surfaces.

Thin film growth methods can be divided into three groups, vapour, liquid and solid phase deposition. Out of these, vapour phase is the most common one used and thus will be the focus in this section. Vapour phase methods can be further divided into two: physical and chemical vapour deposition (PVD & CVD). In PVD, the source material is transported physically from the source to the substrate. This is generally done by vaporizing the compound to be grown using high local temperature

at the source. The generated vapour stream is transported to the substrate without any changes in its chemistry. Examples of PVD include evaporation, sputtering, pulsed laser deposition (PLD) and molecular beam epitaxy (MBE). [11, 13] These methods will be briefly presented later. A special type of sputtering, called reactive sputtering will be presented in more detail.

In CVD volatile species are used, such as gaseous precursors or atomic (or molecular) constituents. They are transported as a stream of vapour to a reaction zone near the substrate. At the zone the precursors react with each other and form the desired compound on the substrate as well as gaseous by-products. For example, AlN can be grown from ammonia (NH_3) and trimethylaluminium (TMAl), and methane is released as by-product. The most common method of causing the reaction is by thermal dissociation, although other methods exist as well. [11] Different variants of CVD exist, including low-pressure CVD and plasma enhanced CVD, along with different CVD based methods such as metal organic vapour phase epitaxy (MOVPE). [11, 13]. CVD methods will be presented below and MOVPE will be discussed in more detail.

Other deposition methods include, for example, different spin-on materials. Sol-gels are an interesting possibility for deposition. They are a colloidal suspension of small particles in a liquid. The deposition can be done by either dipping, spraying or by spin coating. After application the gel is dried and either xerogel or aerogel is formed on the substrate. The former leads to significant shrinkage of the material. In the latter no shrinkage occurs, though the material is roughly 99% voids. [13] Deposition of PZT and other ferroelectric ceramics is possible with this method [15, 16, 17, 18]. What makes this method interesting is that the requirements for crystallinity and orientation of the material are less strict. The piezoelectric properties of PZT can instead be poled with an electric field after deposition [2, 3].

However, the thickness of films deposited by spraying sol-gel is in the range of tens to hundreds of micrometres and the piezoelectric coefficients are significantly lower compared to bulk values [18]. Thinner films have been produced by using spin coating, although such films are still thicker than films produced with vapour methods [16]. Moreover, with high temperature annealing piezoelectric coefficients closer to bulk have been achieved [15].

The main problem in spin coating is that it results in flow like profiles. This results in poor conformal coverage for large structures, such as planned here. [13] Other option would be to completely fill the trench with the piezoelectric material and etch it to desired thickness. This would require accurate alignment and process control. In conclusion, while this method can be used in manufacturing piezoelectric actuators, it is not suitable for this work.

4.1 Physical Vapour Deposition

Evaporation is a common method of PVD and perhaps the simplest of them. The source material is heated up past its melting point and vapour is formed. The vapour is transported in a vacuum to the substrate where it solidifies. Even though evaporation is a simple method it has its limitations with respect to available materials. For

example, evaporation of high melting point elements is difficult. In evaporation, the growth rate depends on the vapour pressure of the source material. For this reason, elements with low vapour pressure are not suitable for evaporation because of infeasibly low growth rates. Moreover, growth of compounds is very limited with evaporation. [11]

AlN can be grown using special evaporation methods. Single crystalline AlN has been successfully grown on sapphire with reactive evaporation of aluminium in ammonia gas using substrate temperatures above 1 000 °C [19]. It is also possible to grow AlN without additional substrate heating by bombarding the substrate with nitrogen ions during aluminium evaporation. Although, the results were polycrystalline and no preferential orientation existed. [20] Especially in the case of ion beam assisted deposition, evaporation is a line-of-sight growth method. As a result, the step coverage is most likely inadequate [13].

With sputtering it is possible to deposit even high melting point materials, as heat is not used to generate the required vapour. Instead, ion bombardment is used to eject atoms from a material target. The ions are formed in a low pressure gas, such as argon, by a strong electric field. A glow discharge is created, in which positively charged ions are accelerated by the electric field and hit the target cathode. The cathode is made of the material to be deposited. As a result, target atoms gain enough energy from the ion bombardment to leave the surface and condense on the substrate. [11]

By introducing a reactive gas into the systems, it is possible to grow compound materials. For example, oxides and nitrides can be made by providing a supply of oxygen and nitrogen, respectively. AlN can be deposited by sputtering aluminium under nitrogen atmosphere. This method is called reactive sputtering and it will be discussed later in Section 4.3 along with more details about sputtering. Sputtered films are typically polycrystalline. However, they can be made single crystalline by solid phase epitaxy after sputtering by annealing. The main parameter affecting the crystallinity of the film is the substrate temperature with respect to the melting point. [11]

Typical substrate temperatures for AlN deposition range from room temperature to 500 °C [21, 22]. Though even without additional heating, the self-heating of the plasma and ion bombardment increases the temperature of the substrate to approximately 100 °C [23]. Commonly used deposition pressures range from roughly 100 mPa to 3 Pa. Generally, lower pressures are optimal for AlN deposition. [22, 23, 24, 25] The effect of deposition pressure will be further discussed later in Section 4.3. Reported deposition rates range all the way from a few nanometres per minute to micrometres per minute [24, 26].

PLD uses a laser to vaporize the target material. A vapour plume is formed that rapidly expands towards the substrate. The plume formation is a multi-step process, as the interaction between the laser and the target is complex. The energy in the laser excites both electrons and phonons in the target. The phonons in turn lead to a molten layer at the surface, which then evaporates. Vapour and molten material is ejected as a result. In addition, plasma is formed and exfoliation of material occurs. [11]

Due to the combination of the previously listed mechanisms the ejected plume contains atoms, molecules, electrons, ions, clusters, solid particles and molten globules. The micrometer-sized particles are the main drawback of PLD. Moreover, the ejected plume is small in size, thus this method is not suitable for large scale production. In addition, the uneven distribution in the plume leads to non-uniform film thickness over the substrate. [11]

In PLD, the vacuum and power source are decoupled. This adds flexibility to the method, enabling different operational modes compared to other growth methods. Reactive growth environment is also possible, as in reactive sputtering and PLD can be combined with other evaporation sources. Other advantages include high deposition rates and the possibility to make multicomponent films with good stoichiometry. [11]

MBE operates far from the thermodynamic equilibrium and the growth is governed by surface kinetics. MBE differs from other deposition methods by its use of ultra-high vacuum of less than 10^{-7} Pa. At this pressure, the mean free path of the molecules is greater than the distance from the beam source to substrate. The transport of the reactant gases is changed from viscous flow to molecular beams. Speciality of MBE are in situ surface diagnostic methods, which enable accurate control of the growth. This method is line-of-sight as well, though atoms on the surface can diffuse, improving the conformal coverage. [11]

All PVD methods are generally line-of-sight methods, depending on the pressure and distance from source to the substrate. This means that the precursors travel along a line-of-sight path from the source to the substrate. As such, growth rate on vertical sidewalls is significantly less than on horizontal surfaces. Some material is deposited on the walls, and some diffuses from other surfaces. In addition, the substrate can be tilted to increase the growth rate on vertical surfaces. However, in this case the aspect ratio is limited and only one side of the actuator beam is covered at a time. For these reasons, other methods for growth on side walls are required. [11]

4.2 Chemical Vapour Deposition

CVD covers various different chemical systems for crystal growth. The systems are based on transport of volatile chemicals, mostly halides, oxides, hydrides and metal-organic compounds. CVD is well suited for mass scale production because it is a batch process and there is no inherent limit in wafer sizes. CVD in itself is a growth method with different realizations such as low pressure and plasma enhanced CVD. Moreover, more specialized variants utilizing same principle exist. These include atomic layer epitaxy (ALE) and MOVPE. [11]

In principle, CVD works as follows. Components of the crystal to be grown are supplied as a volatile compound and transported to a substrate. There elimination reaction occurs leading to crystal growth at the surface. There are three different mechanisms for the elimination reaction: disproportionation, hydrogen reduction and thermal decomposition. For thermal decomposition the substrate is heated to high temperatures. [11]

In principle, the conformal coverage of CVD methods should be excellent. The precursors gasses should react only on the surface of the substrate. If the precursor gasses are able to flow into the trenches and other features on the surface at a sufficient rate, the film should grow on all surfaces. Of course, the growth rate will be slower in places where the precursor gasses cannot flow or diffuse efficiently into. [11]

The purpose of a CVD reactor is to provide a platform for the substrate(s), heating and source gases. Several reactor configurations exist for this purpose, four of which are presented here. In a horizontal reactor, the substrate is in horizontal orientation and the precursor gases are introduced from the side. The gasses flow over the substrate parallel to it. In vertical reactor the substrate is in the same orientation. However, the precursors come from above the substrate and flow perpendicular to it. [11]

An upside-down reactor is basically a vertical reaction turned upside-down. Thus, the precursors flow from beneath the substrate. The substrate must be fixed in some way so that it does not drop. This type of reactor has one advantage over the previous types. If particles form in the gas phase due to parasitic reactions, they will not end up on the substrate as likely. The last reactor configuration is the chimney type. It is especially suited for large scale production, as it can accommodate multiple substrates at the same time. In this reactor, the substrates are held vertically on the walls of a cylinder. The precursors flow parallel to the surface. The last two reactor configurations offer better growth uniformity. However, the difference caused by the configuration alone is not significant. [11]

As the growth rate is determined by chemical reactions and mass transport, it is important that the temperature and transport profiles are both uniform over the substrate. Otherwise the growth will be uneven across the substrate. The gas flow should be in the laminar or near the laminar flow regime. Rolls and vortices should be avoided. Total flow rate of gasses affect the temperature profile above the substrate due to different heat transport mechanisms. [11]

Out of the three different mechanisms, conduction and convection are affected by flow rate. At high flow rates convection of heat defines the temperature profile, whereas conduction dominates at low flow rates. Depending on the reactor type, radiative heat from the substrate can increase the temperature of the gas source or reactor walls. At high flow rates a boundary layer can form over the substrate. The temperature is high above the substrate and decreases rapidly due to heat convection. The temperature increases again as the gas is heated by a gas source or reactor wall, which in turn are radiatively heated by the substrate. [11]

In addition, the carrier gas selection affects the temperature field as well. Commonly used carrier gasses nitrogen and hydrogen have significantly different thermal conductivities. Using nitrogen, which has a lower conductivity, leads almost definitely to a formation of a boundary layer and in turn more uniform growth. In conclusion, with respect to uniformity of the growing film, high flow rates and low pressures are desired. [11]

With ALE, III/V compounds can be grown by using self-terminating layer by layer growth. The precursor gasses are introduced one at a time in pulses and the

chamber is purged using inert gas between precursor pulses. Moreover, the precursors used can only react at the surface and quickly saturate it. Thus, only one atomic layer (monolayer) grows per cycle. [11] ALE offers almost perfect control of film thickness down to atomic layer accuracy. The film should also grow at the same rate on each surface. [13] This should make ALE well suited for this work. However, growing crystalline films with ALE is difficult. In addition, ALE films are known to contain impurities as incorporated by-products. The piezoelectric properties of such films would be too low or even non-existent. [27]

MOVPE uses, as the name implies, metal organic compounds as precursors for growth. One of the advantages of the compounds is their lower decomposition temperature compared to other alternatives. Lower growth temperatures have made possible sharper interfaces in heterojunction devices. MOVPE is a very versatile and broadly used method for the growth of high quality epitaxial layers. Most III/V and II/VI compound semiconductors can be grown. It is especially suited for mass scale production. [11] This method will be presented in more detail later.

Considering the requirements for sidewall coverage and crystal quality, only MOVPE fulfils them both. ALE can meet the side wall coverage requirement. However, the crystal quality could be a significant problem.

4.3 Reactive Sputtering

Reactive sputtering differs from normal sputtering that in addition to the ion source gas, another gas is introduced into the system. This reactive gas serves as a source for second element in compound films, such as nitrides and oxides. It is suitable for wide range of epitaxial materials, including metals and alloys, elemental and compound semiconductors, and oxides. The pressures used range from roughly 1 to 100 Pa. For higher quality films even lower pressures of 1 mPa to 100 mPa are used. [11] For AlN deposition pressures from 100 mPa to 3 Pa have been reported [22, 28].

There are other variations to the basic reactive sputtering method described earlier. In bias sputtering, a voltage is connected to substrate. This method is sometimes called ion-plating as well. Due to the biased substrate, it is ion bombarded before and during deposition. This bombardment cleans the surface by knocking loosely bound atoms. It also leads to low-energy ion implantation and better adhesion of the film. In addition, desorption of gasses occurs. Bias sputtering leads to better conformal coverage than normal sputtering. Some properties of bias sputtered films are different compared to normal sputtered films. [11]

For reactive sputtering DC-biasing the substrate is not optimal, as it leads to some problems. Because oxides and nitrides tend to be insulating this causes build up of surface charges. This in turn reduces the ion bombardment. The solution to this issue is RF or pulsed biasing, which eliminates the build up. [11]

For generating the positive ions required for sputtering, the simplest method is to use a glow discharge. The type of the glow charge depend on the gas pressure, voltage, electrode configuration, which affects path length of the discharge and current density, and current-voltage characteristics. Currents used range from 1 nA to 10 A. [11]

The glow formed between the cathode and anode contains eight different regions.

Near the cathode the released electrons have not gained sufficient energy from the electric field to make ionizing collisions. This creates the Aston dark region near the cathode. As the electrons travel further from the cathode they gain enough energy for ionization. In this cathode glow region visible glow is observed. After travelling far enough from the cathode the electrons have gained significantly more energy than is required for ionization. At this region no visible glow is observed, even though the gas is ionized, because the surplus energy is released as UV-radiation. This creates the Crooke's dark region. Most of the ionization in the system occurs in this region. After the electrons have gone through enough collision they cannot ionize the gas any more. However, they still have sufficient energy for excitation of bound electrodes and this creates a negative glow region. After this region comes Faraday and positive column dark regions, followed by anode glow region. [11]

Continuous source of electrons from the cathode is required to keep the gas conductive. Moreover, sufficient electron multiplication through ionization is needed for steady state conditions. The electron mean path is inversely proportional to the gas pressure. Thus the distance an electron needs to travel before ionizing collision is inversely proportional as well. The thickness of the Crook's dark region increases with increasing pressure. If pressure is too low, this region will shift to the anode resulting in no glow and the discharge will be extinguished. As a result, for low pressure sputtering supplemental mean for discharge or increase in electron trajectory is required. [11]

RF excitation is one way to supplement the discharge. Another method is to use a hot cathode, which provides increase of electrons via thermal emission. Instead of increasing the emission of electrons, their trajectories can be increased by using a magnetic field. In the field the electrons take a spiralling path increasing the length of the trajectory. [11] Because growth of c-axis oriented AlN typically requires low pressures, magnetron sputtering is a popular method [22, 23].

The sputtering growth rate Q is given by the equation

$$Q = CI\gamma, \tag{22}$$

where C is a constant depending on the sputtering apparatus, I is the ion current and γ is the sputtering yield. The yield is a function of the voltage and ion used. Argon ions are most commonly used, due to good yield and inertness of argon gas. From Equation (22) follows that for high growth rate maximum current should be used. Though this is only true up to a point due to the complexity of the system. Also, power limitations might prevent increase of current. Increasing the pressure also increases the current. However, it also increases the probability that sputtered atoms will diffuse back. Thus, after a certain point increasing pressure will decrease the growth rate. Approximately, at pressure of 100 Pa only 10% of the atoms travel past Crooke's region. [11]

The substrate positioning affects the growth rate as well. In principle, it should be positioned as close to the cathode as possible in order to collect the sputtered material. However, the substrate cannot disturb the glow discharge. Moreover, moving the substrate towards the cathode will decrease the current even before Crooke's region is reached. [11]

With respect to crystal growth, the following aspects need to be considered. Influence of the inert gas pressure, energy of the sputtered particles and bombardment of the crystallizing phase by charged particles. Typically, sputtered films are polycrystalline. Subsequent annealing can turn the sputtered films into single crystalline in some special cases. [11]

Reactive sputtering has been the main method for growing *c*-axis oriented AlN. Magnetron sputtering has been almost exclusively used in both RF and DC modes. For DC sputtering, the biasing is typically pulsed in order to avoid the build up of surface charges [21, 28]. Piezoelectric AlN has been successfully grown on silicon, glass and metal substrates, as well as on most electrode metal thin films on Si [24, 29]. Reported deposition rates range from 4 nm/min to 3 μm/min [24, 26]. Generally, the crystal quality of sputtered AlN films is not the best achievable. For good *c*-axis orientation of the film, low deposition pressures should be used [22, 23, 24, 25]. The pressure itself is not the reason for the textured growth of AlN, but the relationship between the mean free path of the sputtered Al atoms and the distance from target to the substrate.

(002) oriented growth of AlN is favoured when the mean free path is greater than the distance from target to substrate. In other words, the atoms generally arrive on the substrate without making collisions first. On the other hand, if the distance from target to substrate is greater than the mean free path, (100) oriented growth of AlN is favoured. Thus, low pressures and short distances should be used for *c*-axis AlN deposition. [22, 23, 24, 25] Under these conditions, the deposition is a line-of-sight method, which is generally not desired for conformal coverage of the sidewalls. As a result, there is an inherent trade-off in sputtering between good textural orientation and sidewall coverage.

Better deposition on the sidewalls could be achieved by tilting the substrate. However, because the arrival of the incoming atoms is highly directional, instead of diffuse, the film growth is also directional. The orientation of the film depends on the angle of the arriving atoms, not on the orientation of the substrate. As a result, the AlN grains will be tilted with respect to the sidewall surface, as can be seen in Figure 7 [30]. This reduces the efficiency of the electromechanical coupling because the electric field cannot be aligned parallel to the *c*-axis.

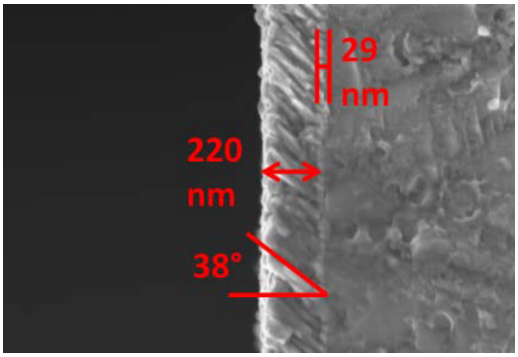

Figure 7: Result of AlN sputtering on vertical sidewalls by tilting the substrate. The columnar grains of AlN are tilted with respect to the surface. [30]

In conclusion, good crystal quality, deposition on sidewalls and high electromechanical coupling cannot be achieved simultaneously with sputtering. AlN deposition and sidewall growth can be clearly done with sputtering. However it is not the optimum method for this work.

4.4 Metal Organic Vapour Phase Epitaxy

MOVPE is a versatile method capable of growing a wide range of different solid materials. It combines fast growth rates and good quality of films. It is used in the growth of different III-nitride compounds, especially for LED devices. However, it has not been used in the MEMS field so far. MOVPE can be used to grow high quality crystalline or polycrystalline thin films. Moreover, film growth in MOVPE reactors is a batch process and single reactors can take in several wafers at the same time. Thus, the method is suitable for industrial scale production. [11]

The main focus of MOVPE grown AlN has been in using it as a buffer layer for GaN growth. However, some studies exist in growth of high quality AlN with MOVPE. [31, 32]

The basic concept is the same as in other CVD methods. A mixture of precursors and carrier gases flows in to a reactor chamber where heated substrate or substrates are. Only the substrate is heated in order to avoid decomposition and growth on the reactor walls. As a result, a film of desired material is grown on the substrate. Typically used pressures range from 1 kPa to atmospheric pressures. Low pressures are preferred because they yield laminar flows and uniform temperature fields, leading to more uniform growth. [11]

Where MOVPE differs from other CVD methods is the precursors used for group III elements. Organometallic liquids are used and they are transported into the reactor as vapour. This is explained in more detail later. Hydrides are used for group V elements. The general chemical reaction for III-V semiconductor growth is

$$\mathrm{A^{III}R_3 + B^{V}X_3 \rightarrow A^{III}B^{V} + \text{organic by-products}}, \tag{23}$$

where R is an alkyl or other organic group, X is typically an hydrogen atom or in rarer cases an organic radical or a halogen atom. A and B are the cation and anion, respectively. Naturally, most MOVPE processes are more complex than the equation above. [11] For AlN growth, TMAl and ammonia have been used as the precursor gasses with hydrogen as the TMAl carrier gas. The growth reaction is

$$\mathrm{Al(CH_3)_3 + NH_3 \rightarrow AlN + CH_4}. \tag{24}$$

However, this reaction is greatly simplified and the actual reaction involves several steps and intermediary reactions, as seen in Figure 8. [33]

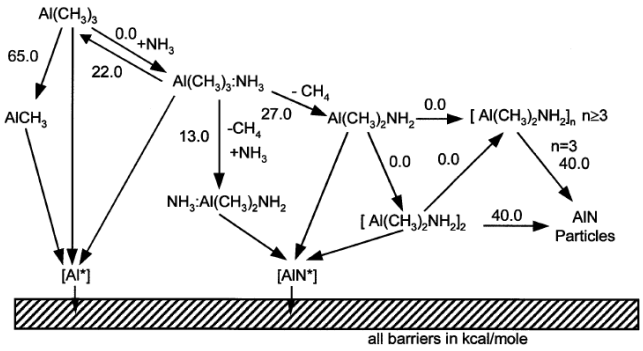

Figure 8: AlN growth reaction. [33]

The growth rate in MOVPE is mainly determined by two factors. The first factor is the gas phase transport of precursors or their reaction products to and from the substrate. The second one is the chemical reactions near or at the interface. These reactions convert the precursors to group III and V atoms and also incorporate them into the growing lattice. The process is illustrated schematically in Figure 9. Both factors have different temperature dependencies. Precursor transport to the substrate is mainly governed by diffusion, which is only weakly dependent on temperature around typical growth temperatures. Chemical reactions on the other hand are exponentially dependent. [11]

However, the growth rate does not increase exponentially with temperature. There is a limit after which the growth rate begins to decrease as temperature increases. This occurs because desorption of atoms from the surface increases. Moreover, predeposition on reactor walls as well as gas phase parasitic reactions increase. These three mechanisms lead to overall decrease in growth rate. [11]

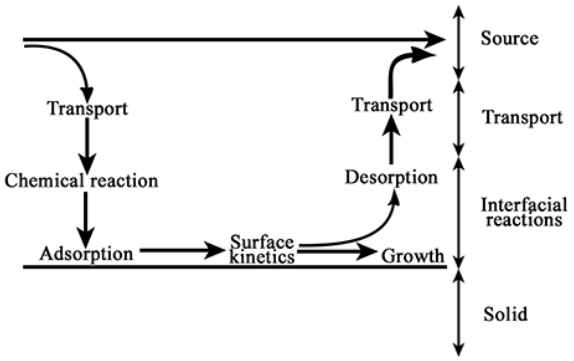

Figure 9: Transport and reactions in the MOVPE growth process. Adapted from [34].

Because the growth rate is determined by transport and reactions, it can be also limited by them. When the growth is mass transport limited the growth rate is independent of the temperature. This can occur in two ways. At high temperatures when chemical reactions are faster than transport or at low precursor partial pressure.

Reaction limited growth occurs when transport is faster. This typically requires low temperatures or large partial pressures of the precursors. The surface kinetics of adsorbed atoms may also limit the growth rate under the same conditions. [11]

If the growth is mass transport limited, the growth rate is linearly dependent on the group III precursor supply. In most MOVPE processes this is the case. The growth rate can saturate at a combination of low temperature and high partial pressures due to higher supply of precursors than what can be incorporated. [11]

In MOVPE, three of the reactor designs are commonly used. They are horizontal, vertical and planetary designs. In the latter two, the substrates are rotated. In vertical rotating disk reactor, the substrate or substrates are attached to a disk named susceptor. The disk rotates roughly 1 000 times per minute. The gas inlet is over the substrates. The fast rotating speed forces the streamlines parallel to the substrate surfaces. This provides more uniform growth rates over the susceptor. In planetary reactor both the substrate holder and substrates rotate. Reactants are introduced from the top as in vertical reactor. Rotation speeds are considerably lower, 0.5 and 5 Hz for the holder and substrates, respectively. The rotation of the substrates is commonly done using a gas foil, which lifts and rotates them. The two rotation modes combined with the gas introduction from the top provides a uniform and stable distribution of precursors. This yields uniform growth rates over one substrate as well as between different substrates in the same reactor. [11]

The gas-vapour delivery system in MOVPE differs from other CVD systems. The organometallic liquids used as a precursor for group III elements require vaporization and transport to the reactor using a carrier gas. This is done by using devices called bubblers. They are temperature controlled baths, through which the carrier gas flows and picks up precursor vapour. The amount of vapour picked up depends on the vapour pressure of the precursor. Because the vapour pressure is temperature dependent, the temperature needs to be kept constant for a constant flux of precursor. The carrier gas needs to spend enough time in the bubbler as well in order to reach the equilibrium vapour pressure. The partial pressure of the precursor p_{gp} in the reactor is

$$p_{gp} = \frac{Q_{lp}}{Q_{tot}} \frac{p_{reactor}}{p_b} p_{vap}(T), \tag{25}$$

where Q_{lp} is the gas flow through the bubbler, Q_{tot} is the total gas flow into the reactor, $p_{reactor}$ is the reactor pressure, p_b is the bubbler pressure and $P_{vap}(T)$ is the equilibrium vapour pressure of the liquid at bubbler temperature T. [11]

Delivery systems for gaseous group V precursors are the same as in other CVD systems. The partial pressure for those is

$$p_{gp} = \frac{Q_{gp}}{Q_{tot}} p_{reactor}, \tag{26}$$

where Q_{gp} is the precursor flow. The gas flows are commonly controlled using thermal mass flow controllers. All gasses, gaseous and vapour, are fed together into the reactor, and exit through a controlled vent. [11]

Decomposition of the precursors is an important and a required part of the process. It can happen through any type of energy transfer, thermal decomposition (pyrolysis)

being the most common. Other possible types are plasma and photodecomposition. In the former, ions of the plasma collide with the precursor molecules breaking them. In the latter, high energy photons break the chemical bonds in the molecules. These methods are attractive alternatives to thermal decomposition due to significantly lower growth temperatures. This would enable more flexibility in process integration. However, the non-thermal methods have not been successful so far. The produced crystal quality is not as good when compared. For example the ion bombardment causes damage and surface mobility is not high enough due to lower temperatures used. [11]

Thermal decomposition temperature (T_{50}) of a precursor is its most important property along with vapour pressure. It is defined as the temperature where 50% of the precursor molecules have decomposed. The decomposition temperature interval for a typical precursor is between 50 K and 100 K. The decomposition temperature defines the substrate temperature required for adequate decomposition rate. Selecting precursors with low decomposition temperatures lowers the required growth temperature. However, this increases the rate of predeposition reactions. Moreover, with low growth temperatures the surface mobility might not be enough for epitaxial growth. Thus, there is a lower limit for useful decomposition temperatures. Ultimately, the upper limit is set by the temperature tolerance of the susceptor. Useful decomposition temperatures are between 500 K and 900 K. [11]

Decomposition can happen in both gas phase or at the substrate surface. Reactions in the gas phase are called homogeneous and at the surface heterogeneous. The latter is often the dominant type. The condition of the reactor walls influences the growth and quality of films as well. Impurities from previous growth processes can be incorporated in the growing film, affecting its properties and quality. Another source of possible impurities are the decomposition by-products. The pyrolysis of hydrocarbons release carbon radicals that are easily incorporated. Hydrogen is also adsorbed and it reacts at the surface. The reactions and rates are mostly unknown due to complexity of pyrolysis reactions. Moreover, other precursors and the presence of different surfaces also affect the process. Even though the whole process is complex, ultimately the relevant factors are: which molecules reach the substrate, does surface reactions eliminate the last attachment of the desired atoms and do the atoms have enough mobility on the surface for epitaxial growth. [11]

Important process parameters in MOVPE include for example substrate temperature and material, reactor pressure, precursor and carrier gas flows and V/III ratio. The growth rate of the film, surface quality and crystallinity all depend on the previous parameters. For AlN growth, it has been reported that increasing Al supply and decreasing V/III ratio increases the growth rate [35]. Moreover, decreasing the V/III ratio increases the film quality with respect to surface roughness, film uniformity and crystallinity [35]. The film quality can be increased by increasing the temperature and decreasing the pressure as well [36]. The root cause behind the changes is attributed to the increased diffusivity of the Al source molecule in gas phase and on the substrate surface. Diffusivity increases in high temperatures and under low pressure, towards which the reactor pressure and ammonia flow count.

5 MEMS Gyroscopes

The planned actuator discussed in this thesis is designed to be used as a part of a MEMS gyroscope. In previous sections, the piezoelectric parts of the actuator were discussed. In this section, other parts of the actuator and the gyroscope device will be presented. Main focus will be on the selection of the electrode material. In addition, a possible fabrication method for the actuator beam will be presented. Next, a brief explanation of the operating principle of MEMS gyroscopes is given.

A gyroscope measures how fast an object turns. They are used in applications such as inertial navigation, automotive chassis control, image stabilization and nowadays in user interfaces for human-computer interaction. Previously, rotating wheel or optical gyroscopes have been used. However, for automotive and consumer applications they are too large and expensive. In comparison, MEMS gyroscopes are lighter, smaller and cheaper. [1] Thus, they have found their way into small consumer devices such as mobile phones and game consoles as well.

The operation of a MEMS gyroscope is based on energy transfer between two orthogonal vibration modes. The first mode is actuated and the second one is measured. The modes are named drive and sense, respectively. When the sensor is at rest, the modes are not coupled together and the sense mode does not vibrate. However, when the sensor rotates, the Coriolis effect couples the modes together and the drive mode excites vibration of the sense mode. Then the angular velocity can be defined by measuring the sense mode vibration. [1]

The Coriolis effect causes acceleration according to equation

$$\frac{d^2\mathbf{x}}{dt^2} = -2\boldsymbol{\Omega} \times \frac{d\mathbf{x}}{dt}, \tag{27}$$

where $\frac{d\mathbf{x}}{dt}$ is the velocity of the object in the rotating systems and $\boldsymbol{\Omega}$ is the angular velocity vector. Thus, the Coriolis effect causes movement perpendicular to the axis of rotation and velocity of the object. The velocity term in the previous equation results in the need for actuated drive mode in MEMS gyroscopes. The apparent force caused by Coriolis effect acting on the object is

$$\mathbf{F_C} = -2m\boldsymbol{\Omega} \times \frac{d\mathbf{x}}{dt}, \tag{28}$$

where m is the mass of the object. In the case of vibrating spring, the effective mass should be used. This force can be only seen in the rotating frame of reference. [1]

Currently, typical MEMS gyroscope uses electrostatic actuation and sensing. For the drive mode, comb drive actuators are used. Comb and parallel plate configurations are used for in-plane and out-of-plane sensing, respectively. The drive mode is usually used at the resonance frequency in order to obtain maximum vibrational amplitude. This reduces the required drive signal voltage, and thus power consumption. As mentioned before, compared to electrostatic actuation and sensing, piezoelectric methods do not require DC biasing. Thus, power consumption is lower and signal processing electronics are simpler. [1] Moreover, there are other advantages in using piezoelectric materials, as previously listed in Section 2.1.

5.1 Electrode Material

Common electrode materials used in microelectronics include, for example, aluminium, copper, silver, gold, molybdenum and tungsten [13]. The following requirements need to be considered in selecting the electrode material. Because the piezoelectric material is grown on top of the electrode, the material used needs to promote crystal growth. Mainly, the lattice structure and constant need to be suitable. Moreover, the crystallinity and surface conditions of the electrode affect as well [37]. Thus, selecting only the electrode material is not enough.

The deposition method and parameters need to be selected as well in order to produce desired material properties. In addition, the electrode needs to withstand the growth and other subsequent process steps. Problems may especially arise with high growth temperatures. The electrode growth method needs to meet the same requirements for sidewall coverage as well.

The material selected has to be compatible with other materials used, mainly silicon and the piezoelectric material. However, possible incompatibility problems can be remedied by using diffusion barriers between incompatible materials. For example, copper is incompatible with silicon because they form silicides. Yet, copper is commonly used as a conductor due to its low resistivity. [38] Similarly, incompatible material can be used here if its other properties merit its use. However, this would increase the complexity of the fabrication process.

Moreover, the selected material needs to fulfil other requirements applicable for all electrodes. Generally, good conductivity is not necessary. However, it is advantageous if the material is conductive enough to be used as a conductor as well. This would eliminate the need for separate conductors and both the electrode and conductors can be made in one process. Selecting the electrode material also enables strain engineering between AlN and the substrate. By selecting a material with suitable lattice constant the mismatch between AlN and Si can be accommodated. [13]

The effects of the AlN growth process on the electrode should be considered as well. Growth at a high temperature is effectively annealing the electrode. The microstructure evolution depends on the initial state of the electrode. For polycrystalline films the grains grow during annealing. Amorphous films typically crystallize into polycrystalline films, and in some special cases into single crystalline. [13]

The selection of the bottom electrode material and possible challenges arising from it can be completely avoided if necessary. Instead of using separate metal electrodes, the silicon beam can be used as a common electrode for both piezoelectric elements. While this simplifies the overall process significantly, there is one major drawback. With the common electrode, the piezoelectric elements cannot be operated in the push-pull configuration. This is because the direction of the electric field cannot be changed over the piezoelectric material. Generally, negative voltages are not possible in IC applications. Thus, the elements cannot expand and contract at the same time. The actuation is limited into the other side expanding (or contracting) while the other side remains unstrained by the piezoelectric effect. Thus, there is a clear benefit in using separate bottom electrodes. The actuation force is approximately doubled compared to common electrode configuration.

Commonly used electrode materials with their properties are listed in Table 2. The lattice constant a indicates if growth of single crystalline material is possible, according to Equation (13). The lattice structures should match as well. The lattice mismatch f_{Si} and f_{AlN} with silicon and AlN are calculated using Equation (16). Effective lattice parameter 3.84 Å of (111) silicon is used. The melting point T_{mp} indicates if the material can withstand high AlN growth temperatures. The resistivity ρ is for bulk material. The actual resistivity of a thin film material is typically higher than that of bulk [13]. Lastly, the coefficient of thermal expansion (CTE) is given. A mismatch in CTE between materials is a general reliability concern. Moreover, large CTE mismatches may cause delamination during high temperature processes. On the last row is (111) silicon, which as heavily doped can act as an electrode as well.

Table 2: Commonly used electrode materials and their relevant properties. Source of values is [13] unless otherwise noted.

Material	a (Å)	f_{Si}	f_{AlN}	T_{mp} (°C)	ρ ($\mu\Omega$-cm)	CTE (ppm/°C)
Al	4.046 [39]	0.054	-0.231	650	3	23
Cu	3.596 [39]	-0.064	-0.135	1 083	1.7	16
Mo	3.142 [39]	-0.182	-0.010	2 610	5.6	5
W	3.155 [39]	-0.178	-0.014	3 387	5.6	4.5
Ti	$a = 2.951$	0.055	0.052	1 660	48	8.6
	$b = 4.684$ [40]					
Pt	3.912 [39]	-0.019	-0.205	1 769	10	9
Au	4.065 [39]	-0.059	-0.234	1 064	1.7	14
Si	5.43	-	-0.19	1 414	100[a]	2.6

[a]maximum dopant concentration

For the metals their lattice constant is used to calculate the lattice mismatch. In reality, the effective lattice constant in the growth plane should be used. However, this requires information about the lattice orientation and that the metal film is single crystalline. Thus, the simple lattice constant is used as a guide for lattice matching.

Out of the options, molybdenum and tungsten stand out. Both have small lattice mismatch with AlN, high melting point and CTE close to that of silicon. The small lattice mismatch indicates that they are suitable platforms for AlN growth. Although the lattice structures are not hexagonal. Melting points above silicon mean that they can withstand every realistic growth temperature. Closely matched CTEs mean that thermally induced stresses will be smaller than with other materials. Moreover, AlN has been successfully grown on both materials [37, 41, 42, 43].

Several studies have been conducted on how the metal electrode affects the growth and crystal quality of AlN. Though the interest has been in FBAR and other resonator applications. In all of the studies the growth method for AlN was sputtering. All studies concluded that the metal electrode affects the growth and crystallinity of AlN. However, some disagreement exist on what factors are contributing.

One study found that the electrode material itself was the main factor [29]. The study concluded that materials with face centred cubic crystal (FCC) structure and lattice constant similar to AlN, such as Au and Pt, are the best electrode materials. Metals with body centred cubic (BCC) or hexagonal close-packing (HCP) structures were found out to be the most unsuitable ones. [29]

However, even the best AlN film was of relatively poor crystal quality. Moreover, the different AlN qualities on different electrodes could be better explained by the electrode surface quality. Significant variation between the surface roughnesses of different electrodes existed. Au and Pt with best measured crystal quality had surface rms surface roughness of less than 2.5 nm, whereas other electrodes had roughnesses between 5 and 15 nm [29].

Indeed, other studies have found that there is no correlation between the electrode material itself and AlN quality. The surface of the electrode seems to be the most significant influence on AlN quality. Two main factors are the crystallinity and surface roughness of the electrode. Both Mo and W have been found out to be suitable electrode materials for AlN growth, given that the surface is smooth and the crystallinity is high. Although there are no significant differences between different materials, thus the selection depends on the application and other factors previously mentioned. [37, 43]

From processing point of view, some metals are easier to use than others. For example, Au and Pt, which according to some sources would be the best electrode materials are difficult to etch [44]. In the case of Al, the etch selectivity between Al and AlN could cause problems. Moreover, Al surfaces oxidise quickly. Thus, Mo and W are the two best electrode candidates for this work. Molybdenum is selected out of the two as the electrode material for this work due to available resources.

Unfortunately, both Mo and W readily react with Si at moderately low temperatures. 80 nanometres thick Mo layer reacts completely with Si if annealed at 550 °C for 20 minutes, forming $MoSi_2$ [45]. Similarly, W reacts with Si as well forming WSi_2 [46]. Thus, a intermediate layer is required to prevent these reactions. AlN itself could be suitable for this. Moreover, AlN would act as a seed layer for the electrode, possibly making it more suitable for the final AlN growth. Thus enhancing the crystal quality and piezoelectric properties.

Another material possibility for the barrier layer is SiO_2. It would prevent the reactions between silicon and the electrode metal. Moreover, SiO_2 can be easily grown using thermal oxidation, which has good conformal coverage.

The growth method of the electrode material is an important aspect that should be considered as well. The method needs to be capable of growing the electrode on the sidewalls as well. However, the electrode growth methods are not in the scope of this thesis.

5.2 Beam Fabrication

The quality of the sidewall surface is an important factor in the crystal growth. For this reason, the fabrication of the beam needs to be considered as well. After the beam fabrication, mainly etching, the sidewall surface should be smooth and have

the desired crystallographic orientation in order to provide the best crystal growth results. Obviously, the surface will not be as ideal as the polished surface of a wafer. The goal of this section is to find methods for the fabrication of the beam with sufficient sidewall quality.

One possibility is to use a combination of reactive ion etching (RIE) and anisotropic wet etching in the bulk micromachining. SOI wafer with (110) orientation is used as the substrate. This way, the vertical walls of the actuator beam have the (111) orientation, as shown in Figure 10. The device layer of the SOI substrate forms the actuator beam and the buried oxide layer works as an etch stop. Additionally the oxide layer works as a sacrificial layer that can be etched away later, releasing the actuator beam from the substrate.

RIE can be used to first define the shape of the actuator structure. RI-etching is highly directional and will results in accurately vertical sidewalls compared to other methods. However, after the etching the surface will be most likely too rough for high quality crystal growth. The rough surface can be smoothed using different methods, one of which is anisotropic wet etching. The (111) orientation of the sidewall enables the use of potassium hydroxide (KOH) etchant. KOH etches silicon at different speeds in different directions. {100} and {110} planes etch significantly faster than the {111} planes, which do not etch practically at all. The etching of the beam should terminate to the slow etching {111} plane leaving a smooth surface with the desired crystal orientation. [13]

One drawback of this method is that the KOH can etch the sharp corners of the beam rounding them. However, this might not be a problem since the etching does not need to be long. Moreover, small rounding of the beam upper corners might be advantageous. It will improve the step coverage of the electrode material. This in turn simplifies the electrical contacts to the electrodes. If the electrode material runs continuously from the sidewall to the top of the beam, the electrical contacting can be made by patterning the electrode layers on top of the beam.

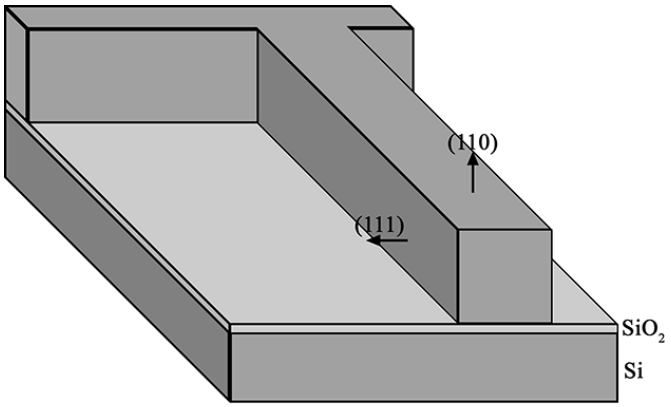

Figure 10: The actuator beam after etching.

6 Characterization Methods

This sections lists and presents the different methods used to characterize the AlN films in this work. The main goal is to define if the crystal quality is sufficient to be used in piezoelectric actuation. The methods presented here are X-ray diffraction (XRD) and scanning electron microscopy (SEM). XRD was the main characterization method in this thesis and is presented in more detail.

6.1 X-Ray Diffraction

XRD is a popular nondestructive characterization method suitable for thin films. In short, it utilizes the reflection of X-rays from a sample in gathering information about material properties. It is possible to acquire information on, for example, lattice parameters, misorientation of the lattice with respect to the substrate and other lattice defects and their densities. In addition, strain, composition and thickness of the film can be determined with XRD. [9] In this section, the theory and basics of XRD are presented. Moreover, how the properties of the sample affect the measurements are discussed.

Heteroepitaxy on highly mismatched substrates leads to either unusually high strain or relaxation of the film through lattice defects, as mentioned in Section 3.3. Despite the strain, impurities and defects, AlN and other III-nitride devices work well and can be analysed using XRD. [9]

In principle, XRD is based on the constructive and destructive interference of X-rays. The sample is analysed using X-rays with a wavelength λ, which should be in the same range as the analysed lattice. Otherwise no interference will be observed. First, each atom in the lattice scatters the X-rays. The bound electrons around the atom cores scatter the X-rays by absorption and emission. Practically all of the scattering is elastic, thus the wavelength of the scattered radiation stays the same. According to Huygens–Fresnel principle, each atom in the lattice acts as a point source for a new wave. [9, 47]

Constructive interference occurs when path difference of different rays equals a multiple of the wavelength ($n\lambda$). From the geometry in Figure 11 the path difference is $2d \sin\theta$. Thus, the diffraction observed from the sample follows Bragg's law

$$n\lambda = 2d \sin\theta, \tag{29}$$

where d is the distance between diffracting lattice planes and θ is the angle between the incident beam and the lattice planes. The angle ω in Figure 11 is the angle between the incident beam and the surface of the sample. Angles θ and ω are equal only in some special cases. It can be thought that effectively the lattice planes in the sample diffract the X-rays and the sample acts as a diffraction grating. Even though in reality atoms are the source of scattering. [9, 47]

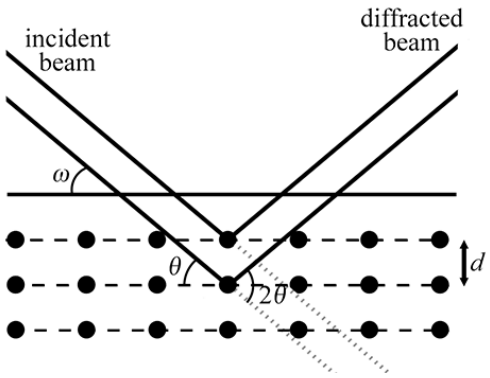

Figure 11: Scattering of X-rays from a crystal lattice. Note that θ and ω are not necessary equal.

By rotating the sample, detector or both in combination diffractions from different sets of crystal planes can be measured. The location of measured peaks correspond to different lattice planes. In experimental setups angle 2θ is measured instead of θ because the detector is aligned to the incoming undifracted beam. [9]

In addition, the peaks correspond to so called reciprocal lattice points in reciprocal space. The reciprocal lattice is a useful construct in many ways and it can be applied to XRD as well. The reciprocal lattice vectors ($\mathbf{g}$) are defined by the real space lattice vectors ($\mathbf{a}$) according to equation

$$\mathbf{g_1} = 2\pi \frac{\mathbf{a_2} \times \mathbf{a_3}}{\mathbf{a_1} \cdot (\mathbf{a_2} \times \mathbf{a_3})}, \tag{30}$$

$\mathbf{g_2}$ and $\mathbf{g_3}$ are cyclic permutations of the above equation [47]. Interestingly, a point in the reciprocal lattice corresponds to a set of lattice planes in real space. The reciprocal lattice points are defined by a vector $\mathbf{G} = h\mathbf{g_1} + k\mathbf{g_2} + l\mathbf{g_3}$. The magnitude of the vector is the inverse of the spacing between $\{hkl\}$ planes. Direction of the vector is normal to the planes. Directions remain the same in both real and reciprocal spaces and distances are inverted. For hexagonal lattices, sometimes a four index Miller's notation $hkil$ is used. The index i is redundant ($i = -(h + k)$) and the three index notation is used in this work. [9]

Using the reciprocal lattice, diffraction can be considered in vector form. A scattering vector $\mathbf{S}$

$$\mathbf{S} = \mathbf{k_h} - \mathbf{k_0}, \tag{31}$$

where $\mathbf{k_h}$ and $\mathbf{k_0}$ are the diffracted and incident wave vectors, respectively, is used to probe the reciprocal lattice. Diffraction occurs when the scattering vector points to a reciprocal lattice point. [9] This is commonly known as the Laue condition ($\mathbf{G} = \mathbf{S}$) and it is mathematically equivalent with Bragg's law (Eq. (29)). Thus, the Laue condition can be interpreted as Bragg diffraction from lattice planes and the waves can be though as if they were reflected from the planes. [47]

By rotating the sample and the detector, the magnitude and direction of $\mathbf{S}$ can be changed. Different lattice points can be found by measuring the intensity of the

diffracted X-rays. The measured diffraction peaks correspond to real space planes. [9]

Not all diffraction spots are accessible though. The maximum magnitude of the scattering vector is $2/\lambda$. Moreover, at low θ angles the sample itself physically blocks the incident or diffracted beams. [9] Some reflections are not allowed because of the extinction rule [47]. There are some special XRD methods, such as transmission and grazing incidence diffraction, which can be used to access some of the otherwise inaccessible spots [9].

For perfect infinite crystals XRD measurements give sharp, narrow peaks corresponding to lattice planes. However, in practice this is never the case and the peaks have definite widths. [9] Next, the various sources of peak broadening are discussed in more detail.

The reciprocal lattice points are broadened by defects in the sample lattice, instrumental resolution, and by the shape and limited size of the sample. In practice, the lattice plane spacings form a distribution. Thus, the reciprocal lattice points cover a finite volume in the reciprocal space. As a result, no sharp diffraction peaks are measured. The peak widths are commonly measured using the peak full width at half maximum (FWHM). [9]

The limited size of sample leads to small X-ray correlation length and is a result of limited film thickness, small grain size and dense dislocations. In addition to dislocations, other defects include tilt and twist of the lattice. Strain and micro-strain cause broadening as well, though those are not discussed here as the film is expected to be relaxed. Wafer curvature is a factor in peak broadening as well, especially if the curvature is not constant over the substrate. All the broadening factors mentioned above are convoluted and their separation is difficult. [9]

The measured lattice parameters can provide information on the strain and stress of the film, as well as information about film composition, CTE and doping. However, there exist severe cross-linkage between these. In addition, reference values are required, such as unstrained lattice parameters, Young's modulus and Poisson's ratio. These values are not accurately known for AlN or for other III-nitrides and they vary from source to source.[9]

There are two possible methods for defining the lattice parameters. The first method is a relative measurement, where the location of the layer peak is compared to a substrate peak. This might not be suitable for AlN due to possible substrate straining. The second method is an absolute measurement, where the location of the peak is directly translated to the lattice parameters. The accuracy can be improved by measuring more than one peak and averaging the results. [9]

For AlN and other hexagonal lattices the separation d_{hkl} between lattice planes $\{hkl\}$ is

$$\frac{1}{d_{hkl}^2} = \frac{4}{3}\frac{h^2 + k^2 + hk}{a} + \frac{l^2}{c^2}, \tag{32}$$

where a and c are the lattice parameters. Because the two lattice parameters are unknown, at least two measurements are needed in order to define both. Parameter c can be defined directly from any symmetrical $00l$ reflection. After that a can be defined from asymmetric reflection using the previously defined c. [9]

The error in d_{hkl} can be defined by differentiating Bragg's equation (29) as

$$\frac{\Delta d_{hkl}}{d_{hkl}} \approx \cot\theta_{hkl}\Delta\theta, \tag{33}$$

where $\Delta\theta$ is the θ step size. Because of the cotangent term, for small error reflections close to $\theta = 90°$ should be measured. However, this could prove challenging because the intensity of the reflections generally decreases as θ increases. In addition, error is caused by unknown temperature and temperature changes. Refraction of the beam causes some error as well, although this error is typically small. [9]

6.2 Scanning Electron Microscopy

SEM is another popular non-destructive method. It uses electrons instead of photons to gather information from materials. The resolution of a microscope is diffraction limited, which is given by the Rayleigh criterion as

$$\Delta x \approx 0.6\frac{\lambda}{\sin\alpha}, \tag{34}$$

where Δx is the resolution, λ is the wavelength and α is the maximum angle of refracted rays from the aperture to the focal point. For large apertures $\sin\alpha \approx 1$ and the diffraction limit becomes approximately 0.6λ. Because of the diffraction limit, the best achievable resolution is approximately 300 nm with optical microscopes using visible light. The resolution can be improved by reducing the wavelength. This can be done, for example by immersing the sample in a high refractive index medium or by using UV or X-ray radiation. [48]

In order to achieve even better resolution, SEM utilizes electrons with a shorter wavelength. In addition to electromagnetic radiation, material particles posses a wavelike character as well. All particles have a de Broglie wavelength λ

$$\lambda = \frac{h}{mv}, \tag{35}$$

where h is the Planck constant, m is the mass of the particle and v is its speed. In SEM, the speed of the electrons is a function of the acceleration voltage defined as

$$v = \sqrt{\frac{2qU}{m_e}}, \tag{36}$$

where q is the elemental charge, U is the acceleration voltage and m_e is the mass of an electron. [48] At a typical acceleration voltage of 15 kV, the wavelength is approximately 10 pm and the diffraction limit is in turn approximately 6 pm.

Even though the diffraction limit would allow it, individual atoms cannot be distinguished in SEM. This is because the resolution is limited by the resolution of the instrument itself. [48]

When a sample is bombarded with electrons, they are either scattered or absorbed by the sample. Both elastic and inelastic scattering occurs. Most of the electrons

scatter into the sample, where they continue to scatter and are finally absorbed. However, a small fraction of electrons are scattered away from a sample or reflected. These electrons can be collected directly in order to acquire information about the sample. [48]

Other method is to collect so called secondary electrons. They are generated in the sample when the incoming primary electrons scatter inelastically. The bound electrons of the sample gain extra energy from the primary electrons and are released from the sample as secondary electrons. The range of different secondary electron energies is wide, which makes focusing difficult. [48]

The focusing can be improved by collecting electrons from a single point at a time. In scanning electron microscopy, as the name implies, a focused beam of primary electrons is scanned over the sample. Both backscattered and secondary electrons are utilized in SEM. The resolution is mainly defined by the diameter of the scanning beam. Typical resolutions are between 1 nm and 10 nm. One added advantage of this method is that the depth of field is large. [48]

The acceleration voltage of the primary electrons affects how deep they penetrate into the sample. The penetration depth is an average over a large number of electrodes and the actual trajectory of individual electrodes is highly different due to the random nature of scattering. The trajectories form a pear shape inside the sample, thus information from this volume is acquired simultaneously. This is also called the electron range R and it is given approximately by

$$R = \frac{aE_o^r}{\rho}, \tag{37}$$

where $a = 10\ \mu\text{g/cm}^2$ and $r = 1.35$ are experimental constants, E_0 is the primary electron kinetic energy in keV and ρ is the density of the sample. Using backscattered electrons, information of the sample is mostly gained from beneath the surface. [48]

The surface of the sample can be studied by using the secondary electrons. The weakly bound outer shell electrons of the sample gain enough energy from the primary electrons to become free. However, they do not have enough energy to travel very far in the sample. Typically they can travel only less than 2 nm. As a results, only secondary electrons released at or very near the surface actually escape the sample and can be collected. [48]

It is also possible to define the elemental composition of a sample with electron microscopy. The tightly bound inner shell electrons in a sample do not take part in chemical bonds between atoms. As a result, their energy states are unaffected and because each element has an unique electron configuration, different elements can be identified. [48]

The primary electrons cause excitation of the inner shell electrons and they move from lower energy states to higher ones. When the electrons de-excite, they return to their original states and release the energy difference as characteristic X-rays. By measuring different emitted wavelengths elemental analysis can be performed. This method is called energy-dispersive X-ray spectroscopy (EDS). Electron beams are one of the methods used for the excitation in EDS. Other methods include X-rays and proton beams. [48]

7 Sample Fabrication and Experiments

In this section, the sample fabrication process and planned experiments will be presented. After briefly presenting the general parts of the fabrication process, the FEM simulations are presented in 7.1. The main part of the sample fabrication was the AlN growth by MOVPE, which is presented in more detail in Section 7.2. The XRD crystal quality measurements are presented in Section 7.3 In addition, Section 7.4 presents the experiments for the study on effects of growth temperature and time on the resulting AlN crystal quality. Growth process for Mo electrode is briefly explained as well in 7.5. In addition, method for calculating particle density and size on the AlN surface is presented in Section 7.6.

For this work, (111) silicon wafers with diameter of 100 mm and thickness of 525 μm were used. The wafers were n-type with resistivity of $8 \cdots 20$ Ω-cm. Because the MOVPE reactor used could only accommodate 50 mm wafers, the 100 mm wafers needed to be cut down. The wafers were diced into 30 by 30 mm samples that were then used as the substrates for AlN growth. The dicing step may have caused some problems in this work, as explained in Section 8.3. For rest of the samples, photoresist protection was used during dicing. After dicing the photoresist was stripped and samples cleaned using acetone, isopropanol and de-ionized water.

7.1 Finite Element Method Simulation

COMSOL Multiphysics 5.1 [49] FEM simulation was used in order to simulate the operation of the actuator. In this section, the simulated models are presented. The models were used to study the difference between the split electrode and sidewall configuration in two different beam geometries. Silicon beams with cross sectional surface area of 6×5 μm^2 and 60×5 μm^2 were used. In conclusion, a total of 4 different FEM models were compared.

How the thickness of the piezoelectric material influenced the actuator performance in both geometries was studied as well. The performances were compared by simulating the in-plane actuator displacements under the same actuation voltage. The results are presented later in Section 8.1.

The 6×5 μm^2 models used are presented in Figures 12a and 12b for the split electrode and sidewall configuration, respectively. The model consists of the silicon actuator beam and of two piezoelectric AlN elements. Other materials and structures are not considered in the simulation. The 60×5 μm^2 models were otherwise similar, however the silicon beam width was 60 μm instead of 6 μm. The beam length was 150 μm for both geometries.

The thickness of the AlN layer was 100 nm in all models. For the split electrode configuration, the width of the AlN layer was 2 μm or 5 μm for the 6 μm and 60 μm beam, respectively. On the sidewall model the corresponding dimension was 5 μm for both beams. In both models the layers spanned the full length of the beam. Other parameters are presented in Appendix A.

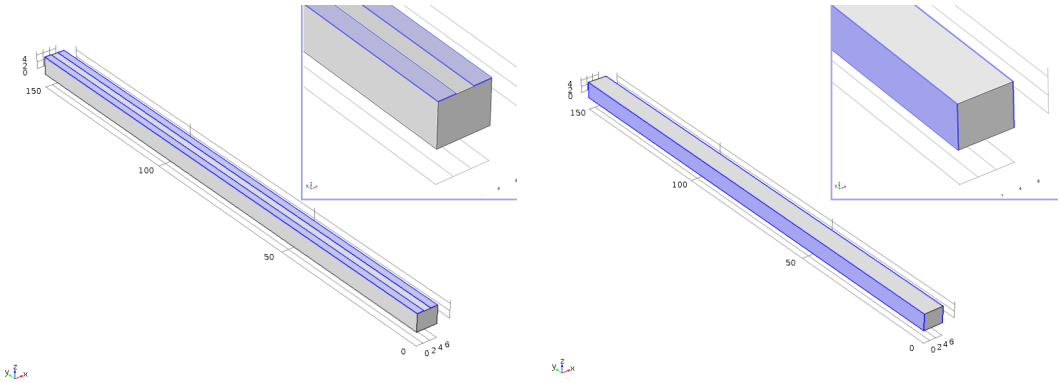

(a) Split electrode configuration. (b) Sidewall configuration.

Figure 12: COMSOL models with the narrow beam used for simulation. The piezoelectric AlN elements are shown in blue.

In all models, the back end of the beam was fixed and all other surfaces were free to move. Electrical ground was defined as the interface between the AlN elements and the beam. Electrical potentials were applied on the top surfaces of the AlN elements. For push-pull mode, actuation voltages of 3 V and -3 V were connected to the right and left electrode, respectively, in all models.

All models were meshed using extremely fine triangular swept mesh. The displacements were solved for a stationary case. In other words the simulated actuators were operated using DC voltage and not at their resonant frequencies. For resonant operation, the damping coefficients are required, which are unknown.

The effect of the piezoelectric material thickness on actuator performance was simulated by varying the layer thickness from 50 nm to 2 μm.

7.2 Aluminium Nitride Growth

AlN was grown in a 3×2" Thomas Swan close-coupled showerhead reactor. The process parameters were based on previous published literature and on a process used in-house in a different reactor. The process parameters are presented in Table 3.

Table 3: MOVPE process parameters used in this and previous work.

Source	Temperature (°C)	Pressure (kPa)	V/III ratio	TMAl flow (μmol/min)	NH_3 flow
This work	1 125	6.67	337	14.59	110 (sccm)
[35]	1 100	5.33	266-34 000	2-60	N/A
[36]	1 100-1 300	6.67-26.66	280-2 000	N/A	N/A
[42]	1 050	2.67	25 000	10 sccm	N/A

The full process flow is presented in Figure 13 and explained in detail next. The process has three main steps. The first step is a bake and nitridation, followed by

AlN buffer layer growth step. The last step is the main AlN growth step. In the first step, the substrate is first heated to 1 065 °C and baked for 5 minutes under hydrogen atmosphere. Then the substrate is baked for another 5 minutes under silane (SiH_4) molar flow of 0.045 μmol/min. The purpose of the first bake is to desorb contaminants from the substrate surface. The silane step deposits a small amount of new clean silicon on the surface. For the nitridation the temperature is lowered to 1 020 °C. Ammonia (NH_3) molar flow of 223 μmol/min is let into the chamber for 15 seconds. Purpose of the nitridation is to prime the surface for AlN growth.

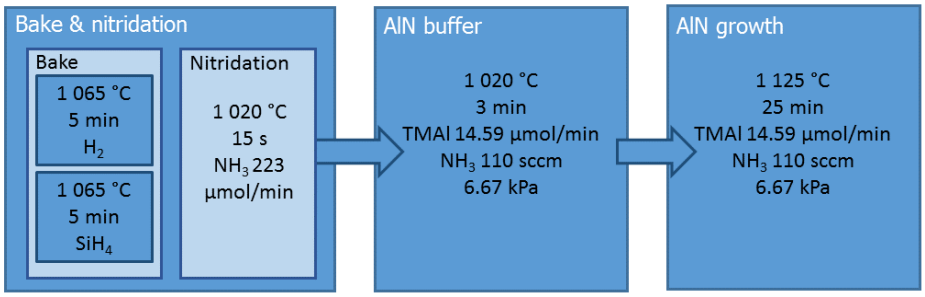

Figure 13: Process flow of the AlN growth by MOVPE used in this work.

Prior to the main AlN growth, a thin low temperature buffer layer is grown at 1 020 °C for 3 minutes. TMAl molar flow is 14.59 μmol/min and NH_3 flow is 110 sccm, giving a V/III ratio of 337. The pressure is kept at 6.67 kPa. For the main growth step other parameters are kept same, excluding growth temperature and time. The temperature is increased to 1 125 °C and the gases flow for 25 minutes.

7.3 X-Ray Diffraction Measurements

In this work, XRD measurements were used in order to define the crystallinity of the AlN film. This was done by measuring the 002 reflection of AlN. The diffractometer used in the measurements was a Philips X'Pert Pro in high resolution (HRXRD) configuration.

In HRXRD configuration, the diffractometer consists of five different components along the beam path, as shown schematically in Figure 14. The X-rays are generated by bombarding copper with electrons in a vacuum tube. Characteristic $CuK_{\alpha 1}$ radiation with wavelength of $\lambda = 1.540560$ Å is generated along with other wavelengths. Next along the beam path is an X-ray mirror, which reduces the beam divergence. Unwanted wavelengths are stripped using a monochromator. It utilizes four germanium crystals and allows only 220 reflections from the crystals to pass through it. Thus it is named 4 × Ge220 monochromator. An analyser is used in front of the detector to reduce the acceptance angle, which in turn increases the accuracy in measuring the 2θ angle of the reflections. Drawback of the analyser is that it reduces the intensity as well. If no analyser is used, the detector is called "open".

In this work, open detector was used for rough alignment of the sample and detector, and a closed detector for the accurate alignment and measurements. The detector is able to rotate along the θ angle and the source is fixed. In addition to the previously mentioned components, a component called goniometer rotated the sample.

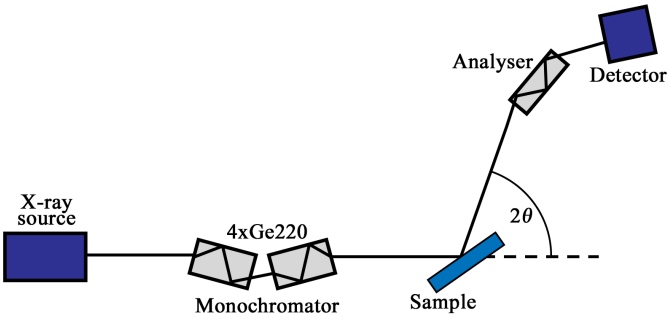

Figure 14: HRXRD measurement configuration. Adapted from [9].

The combination of a rotating detector and goniometer gives a total of 4 rotational axis, which in turn can be used to make seven different types of scans of the sample. The scans used in this work were the 2θ-ω and ω scans. In the 2θ-ω scan the sample and detector are both rotated changing both angles. The angles are kept constant with respect to each other so that $2\theta = 2\omega$. As a result, the magnitude of $\mathbf{S}$ changes while the direction remains the same. In ω-scan a diffraction spot is scanned by changing ω, thus the magnitude of $\mathbf{S}$ remains the same while it traces an arc in the reciprocal space. [9]

The 2θ-ω scan was be used to define the lattice parameters and the ω scans done gave indication of the film crystal quality. As the films in this works are expected to be columnar and mosaic in structure, the tilt of columns is an important factor in the film quality. The columns can be tilted with respect to the substrate and to each other, as illustrated in Figure 15. This would spread the same lattice directions over an angle, thus broadening observed peaks. The lattice tilt can be observed in ω scans of symmetric $00l$ peaks. [9]

Figure 15: Columnar and mosaic film on substrate, illustrating the tilt of the columns, which leads to peak broadening in XRD.

Both 2θ-ω and ωscans were made about the 002 reflection. The detector was aligned to the detector and the sample surface was aligned so that it was parallel with the X-ray beam. After the detector and sample offsets were corrected, the detector and sample were aligned to the AlN 002 reflection.

Both types of scans were done using X-ray source voltage and current of 40 kV and 40 A, respectively. The θ step size was 0.003° in the 2θ-ω measurement and the 2θ angle was scanned over a range of 1°. The ω angle was scanned over a range of 5° in the ω scans, with a step size of 0.014°. Measurement time per step was 5 s in both measurements, resulting in a total measurement time of approximately 30 minutes.

A correlation between the AlN FWHM and the electromechanical coupling coefficient and thus the piezoelectric effect exists. In Figure 16 the relationship between the two is presented from different studies. Four studies used sputtered AlN films and measured the coupling coefficient k^2 using thin film resonator structures in longitudinal mode [21, 37, 50, 51]. One study used MOVPE [42]. The coupling coefficient is defined by equation

$$k^2 = \frac{e_{33}^2}{c^E \varepsilon^S}, \tag{38}$$

where c^E is the stiffness at constant electric field and ε^S is the dielectric constant at constant strain [50].

The FWHM values were defined from a θ-2θ ($\omega = \theta$) scan. The results only indicate the strength of the longitudinal piezoelectric coefficient d_{33} and are not directly applicable for this work. However, these results can be used to give indication of sufficient crystal quality. As can be seen from the results, when the FWHM is below 2° the coupling coefficient is mostly saturated to a constant value. Thus, from application point of view improving the crystal quality beyond the 2° point gives no additional benefits. However, there is deviation in the results and some indicate that the piezoelectric properties could be further improved beyond the 2° FWHM point.

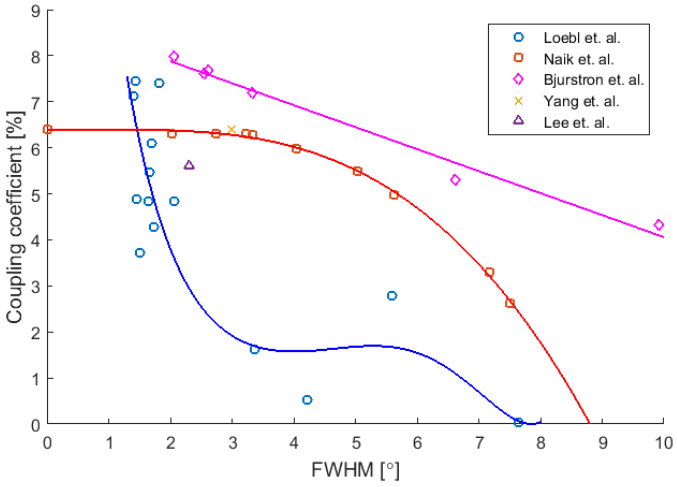

Figure 16: Relationship between AlN FWHM and electromechanical coupling coefficient k^2 from several studies.

7.4 Growth Time and Temperature Experiments

The effect of growth time and temperature on the crystal quality and growth rate was studied. For this purpose, four additional growth times and three temperatures were tested. The times were 60, 90, 120 and 160 minutes while other process parameters remained the same. Temperatures of 750, 875 and 1 000 °C were used.

The thickness of the films was defined by measuring five points with an ellipsometer and then averaging them. The ellipsometer used was Plasmos SD2300 using laser wavelength of 632.8 nm.

From the growth time series the growth rate is determined. Moreover, from the same series the effect of film thickness on crystal quality is determined with XRD. It is expected that as the thickness increases so do the stresses. This in turn generates dislocations and other defects. Ultimately increasing the film thickness may result in worse crystal quality.

Growth temperature is an important aspect in the crystal quality. It is expected that the crystal quality drops with decreasing temperature as well. However, the interesting question is by how much. The crystallinity of the film does not need to be perfect for this application. It would be advantageous considering process integration if the growth temperature could be lowered while still retaining sufficient crystal quality. In addition, the effect on growth rate can be determined from this series as well. The results of both series are presented in Section 8.4.

7.5 Electrode Deposition

In order to study the growth of AlN on Mo electrodes, Mo was deposited using Edwards E306A electron-gun evaporator. Prior to the Mo evaporation, a thin AlN layer was grown using the process presented previously by changing the growth time from 25 min to 12 min. Otherwise the process was the same. Approximately 50 nm of Mo was evaporated on top of the AlN barrier layer under relatively high pressure of 6 mPa. The growth rate was approximately 2.56 nm/min. Before AlN growth the substrate was cleaned again with acetone, isopropanol and de-ionized water. AlN was grown on top of the Mo electrode using the same AlN process with full 25 minutes of growth time.

As previously mentioned in Section 4, evaporation is not a suitable method for growth on sidewalls. However, it was used in this work due to available resources. For actual growth on the sidewalls a more suitable method needs to be used.

7.6 Particle Density and Size Measurement

A Japanese electron optics laboratory (JEOL) JSM-6335F field emission SEM was used in this work in studying the surface of the AlN samples. Secondary electron imaging (SEI) was used. The SEM equipment also had a Oxford Instruments INCA X-sight X-ray detector attached for EDS. The main focus was on analysing particles on the sample surfaces.

The particle density on the AlN was defined by imaging ten locations on a sample with SEM and counting the individual particles seen at each location. The locations

were randomly selected on each sample. The surface area of each selected locations was approximately 27.2 mm^2. Particle density was averaged over the ten locations in order to define the approximate density on a sample. At the same time, the surface of the samples was imagined as well.

A statistical test can be used in order to define if there is a statistically significant difference in particle density between samples. In this work, t-test was used compare two samples in order to see if their particle densities differed. The null hypothesis of a t-test is that there is no difference between the compared values. The probability that the null hypothesis is true p was used in order to decide if there was a difference in densities between two samples. Low values of p indicate that the null hypothesis is false and that densities between compared samples are not equal. [52]

In addition, the average particle size was defined by measuring the diameter of 20 randomly selected particles. Again, t-test was used to define if there was a statistically significant difference between tested samples.

8 Results and Discussion

The results of the sample fabrication, characterization and experiments are presented in this section. First, the results of the FEM simulations are presented in 8.1. The results of the surface characterization of AlN are presented in Section 8.3 along with analysis of the particles observed on the surface.

The main focus of this thesis was the crystal quality of AlN. The results of XRD measurements are presented and discussed in Section 8.2. Additionally, the results of AlN on Mo electrode are mentioned in this section. Lastly, the results of the growth time and temperature experiments are presented in 8.4.

8.1 Electrode Configuration and Actuator Thickness

Here, the results of the FEM simulations of Section 7.1 are presented. The performance of the split and sidewall actuator configuration was compared on a narrow and wide beam. In addition, the effect of the piezoelectric material thickness on actuator performance was studied as well. The purpose of these results are to be qualitative and not quantitative.

The simulated displacement fields are presented for both configurations on narrow beam in Figure 17. The simulated split electrode actuator produces lateral displacement of approximately 21 nm at the actuator end. The maximum lateral displacement in the sidewall configuration on the other hand reaches approximately 53 nm. The simulation results indicate that the sidewall configuration has significantly higher actuator performance.

The bending modes seem identical in both actuators. The twisting of the beam in the split electrode configuration is negligible.

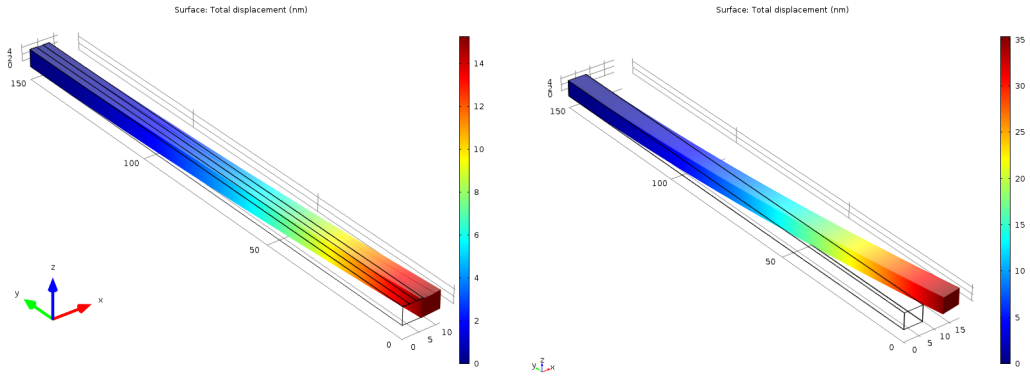

(a) Split electrode configuration. (b) Sidewall configuration.

Figure 17: Displacement fields of the simulated narrow actuator structures. Displacements not to scale.

In Figure 18, the displacement fields for the wide beam are presented for both actuator configurations. There is not a significant difference in lateral displacements between the two configurations. Both produce approximately 0.70 nm of lateral

displacement. However, in the split configuration there was significant twist of the actuator end.

The results indicate that the wider the beam is, the less the placement of the piezoelectric elements matter in actuation performance. This is because the relative difference in the placement becomes smaller. However, in the wide beam the strain of the piezoelectric element also causes twist of the actuator, whereas on the narrow beam this is not observed. This is because on the wide beam the stiffness of the beam is significantly greater in-plane than out-of-plane. Thus most of the stress caused by the strain is relaxed by out-of-plane deflection.

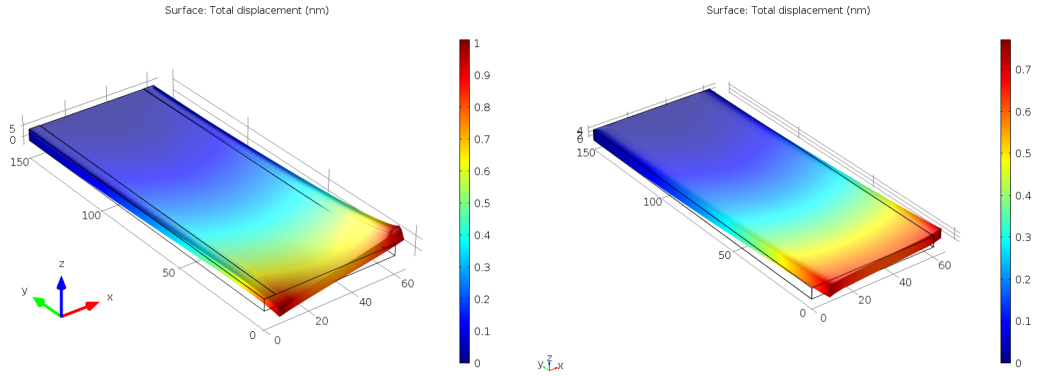

(a) Split electrode configuration. (b) Sidewall configuration.

Figure 18: Displacement fields of the simulated wide actuator structures. Displacements not to scale.

Lateral displacement of the sidewall actuator as a function of the AlN layer thickness is presented in Figures 19a and 19b for the narrow and wide beam, respectively. The results show that the actuator performance decreases as the thickness of the piezoelectric AlN layer is increased. The generated in-plane displacement decreases from approximately 53 nm to 10 nm in the narrow beam, as thickness increases from 100 nm to 2 μm. In the wide beam, the decrease is not as significant. Displacement decreases from approximately 0.70 nm to 0.50 nm.

According to equation (9), the force the piezoelectric element exerts remains constant with respect to the element thickness. The decrease in the lateral displacement according to the simulation results can be explained by the change in elastic properties for the narrow beam. As the total width of the actuator increases with increasing piezoelectric element thickness, the actuator becomes more stiff in the lateral direction. Thus the same force generated by the actuator is able to bend the beam less and less. The change of the actuation displacement then becomes smaller as well. In the narrow beam, the thickness of the elements at thickest was not negligible compared to the beam width (4 μm to 6 μm).

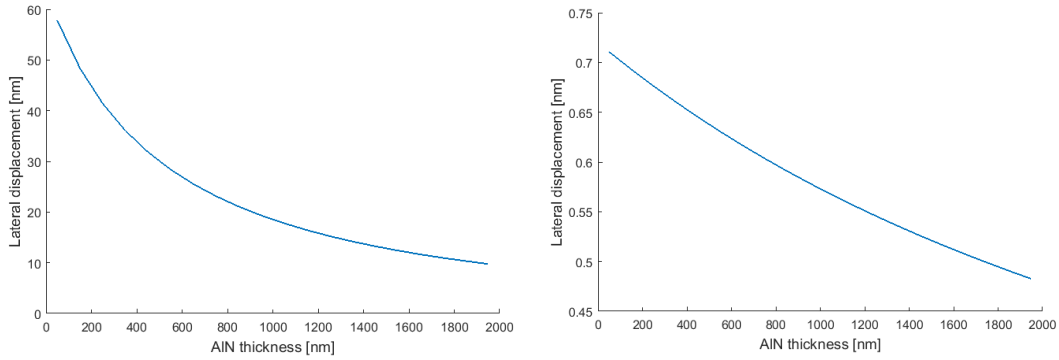

(a) Narrow beam. (b) Wide beam.

Figure 19: The simulated lateral displacement of the sidewall actuator as a function of the AlN layer thickness.

On the other hand, if the silicon beam is significantly wider than the thickness of the piezoelectric elements, their contribution to the overall stiffness of the structure becomes smaller. Then, under constant force the change in the displacement should be smaller. This was the case for the wide beam and correspondingly a smaller change was observed in lateral displacement.

The remaining change in the actuator displacement may be explained by the direction of the force, because it is not in the direction of the deflection. Thus even though the piezoelectric element produces the same force regardless of element thickness, it cannot be said that the force bending the actuator is always the same. Moreover, the generated force also deforms the element and a thicker element is able to deform more, perhaps also leading to reduced performance.

However, even though the results suggest that thinner elements may be slightly better, they cannot be made too thin. The simulation does not account for stress induced failures, such as fracturing or delamination of layers. Neither does it account for dielectric breakthrough of materials. At some point the electric field strength or stress stress caused by the strain of the piezoelectric layer exceeds a point where a failure occurs.

In conclusion, the planned sidewall configuration increases the actuator performance compared to the split electrode actuator. The thickness of the piezoelectric material does not affect the lateral displacement as such. However, it affects the elastic properties of the actuator structure and decreases the displacement by making the structure stiffer.

8.2 Crystal Quality

Results of the XRD 2θ-ω and ω scans of AlN 002 peaks are presented in Figures 20 and 21 for samples without (sample 1) and with surface protection (sample 2), respectively. Interestingly, the sample 1 peaks look sharper compared to sample 2. Although this could be just due to slight misalignment in measuring sample 2. The measured peak full widths at half maximum are presented in Table 4. The values were calculated from the averaged peak, shown in red in the figures.

The results indicate that the crystal quality of the films is relatively good, especially compared to other AlN films deposited by sputtering or MOVPE as previously presented (Fig. 16). The relatively narrow 2θ-ω peaks of the 002 reflection indicate that the piezoelectric properties of the films should be adequate. For sample 2, the peak width of the ω-scan is significantly wider than for sample 1. This indicates that sample 2 has higher density of dislocations and thus more tilt in the columnar grains. Other possible explanation for the result is that the sample was not aligned properly during the scan. This is the more likely explanation, since the growth process on both samples was the same. However, it is possible that the photoresist protection affected the substrate surface, leading to a difference in AlN growth.

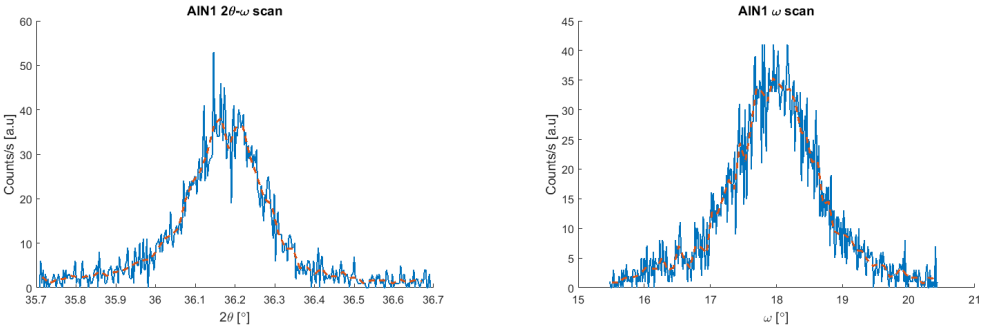

(a) 2θ-ω scan (b) ω scan

Figure 20: XRD measurements of sample 1.

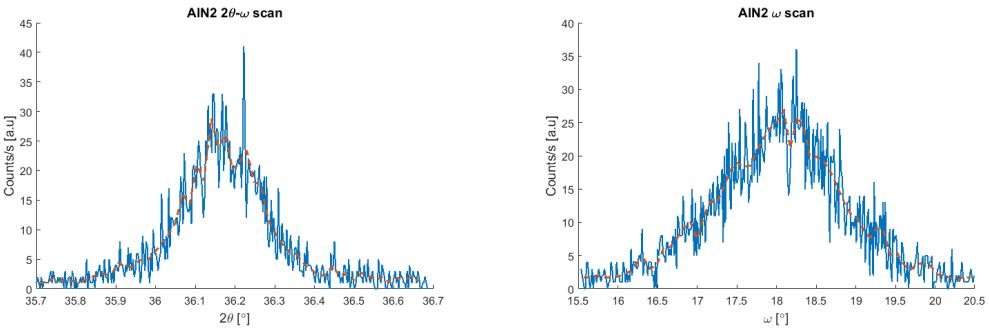

(a) 2θ-ω scan (b) ω scan

Figure 21: XRD measurements of sample 2.

Table 4: Measured FWHM values for AlN 002 peaks.

Sample	2θ-ω (°)	ω (°)
1	0.21	0.51
2	0.19	1.68

The 2θ angle of the peak maxima are at 36.17° and 36.14° for samples 1 and 2, respectively. Using Equations (29) and (32) the angles correspond to lattice parameter c values of 4.963 Å and 4.967 Å. Commonly reported values for unstrained AlN lattice parameter are $c_0 = 4.978 \cdots 4.981$ Å [9]. Thus, it seems according to equations (18) and (20) that the film has out of plane compressive strain of approximately 0.36% and in-plane tensile strain. The in-plane tensile strain could be calculated using Equation (20) if the Poisson's ratio of AlN was accurately known. Unfortunately this is not the case [9]. The critical thickness of AlN on (111) Si substrate is approximately 6.64 Å according to Equation (17). Considering this and the small difference in the measured and reported lattice constants, it would seem the the analysed AlN films were almost completely relaxed. Thus, high dislocation densities are expected.

The error in lattice parameter measurement was ± 0.0002 Å according to Equation (33) with a step size of $\Delta\theta = 0.003°$. However, there are other significant sources of error. As can be seen from the measured curves in Figures 20 and 21 there is noise in the measurements. Moreover, the exact angle of the peak is slightly ambiguous due to the shape of the peaks. Possible misalignment of the sample and the detector to the 002 peak also might have affected the results.

The measured values of the c lattice constant indicate the film was indeed AlN. The chemical composition of the film was confirmed using EDS as well. The measured spectrum is presented in Figure 22. The spectrum indicates that the film contains aluminium and nitrogen. The substrate silicon peak is observed as well. The atomic percentages of the elements could be measured with EDS as well. However, it is not accurate for films this thin.

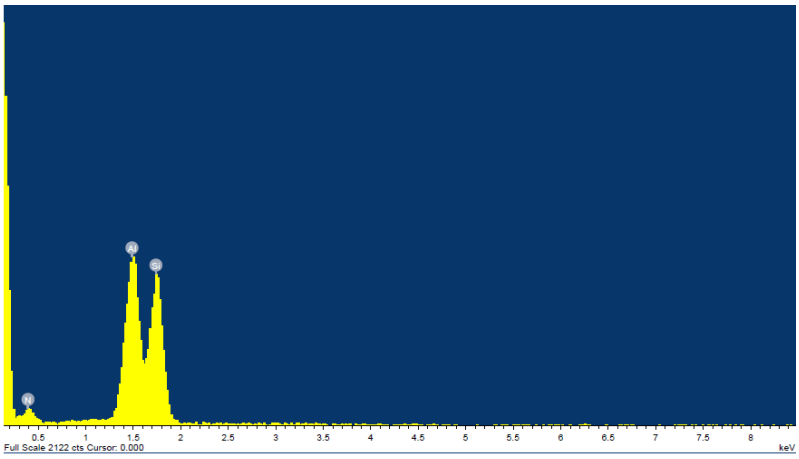

Figure 22: Measured EDS spectrum of the grown film.

The difference in the measured θ and ω peak angles tell the alignment of the c-axis with respect to the surface of the substrate. For both samples, the difference is less than 0.5°. The results indicate that the preferred orientation of the AlN c-axis is almost perpendicular to the substrate surface, as was desired. Moreover, the relatively narrow ω-peak indicates that the distribution of different orientations is narrow as well.

The AlN crystal quality on the Mo electrode could not be determined in this work. The Mo electrode delaminated from the thin AlN barrier layer during the main AlN growth. Parts of the delaminated electrode can be seen in Figure 23. From the MOVPE reactor reflectometry data it was determined that the electrode delaminated during the heating of the reactor at approximately 400 °C.

This could mean that Mo is unsuitable material to be used in high temperature AlN growth. However, because the delamination occurred at a relatively low temperature, the root cause of the delamination was most likely not the temperature itself. Moreover, Mo has been successfully used in a similar process at temperatures above 1 000 °C [42]. Possible causes for the delamination are the poor adhesion of Mo to AlN and the quality of the Mo film itself. The adhesion can be increased by using a more suitable layer under the Mo film. The Mo was deposited using an evaporator under non-idea conditions, which might have resulted in large quantities of impurities in the films. In future research, the deposition method and possible adhesion layer should be investigated.

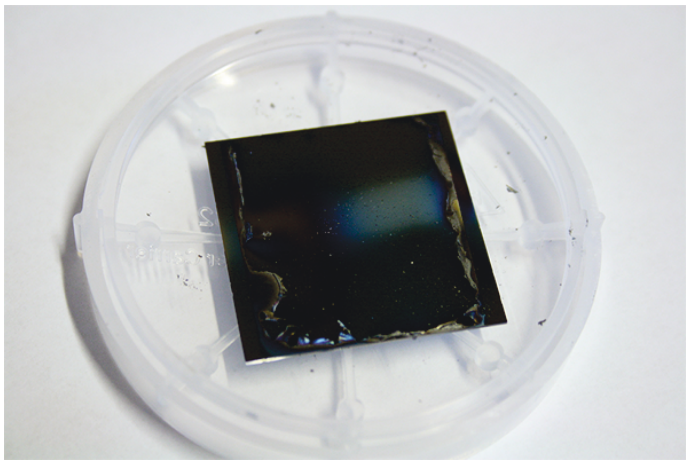

Figure 23: Results of AlN growth on Mo electrode. The electrode delaminated during AlN growth from the underlying AlN barrier layer. Parts of the electrode can be seen at the left and right edge of the sample.

8.3 Surface and Particles

Micrometer sized particles were observed on the surface of the first AlN sample after growth, as seen in Figure 24. The particle was confirmed to be AlN by EDS analysis. Hexagonal hole in the AlN film can be seen around the particle, the silicon substrate is visible through the hole. It was hypothesized that the observed AlN particles were caused at least partially by existing particles on the surface prior to growth. Moreover, it was hypothesized that these particles were generated when the substrates were diced. The existing dicing induced silicon particles may have acted as a nucleation site for AlN growth, resulting in the observed particles. Moreover, the site could have deprived the surrounding area from precursors, resulting in the observed hole in the film around the particles. Other source for the AlN particles could be possible gas-phase parasitic reactions.

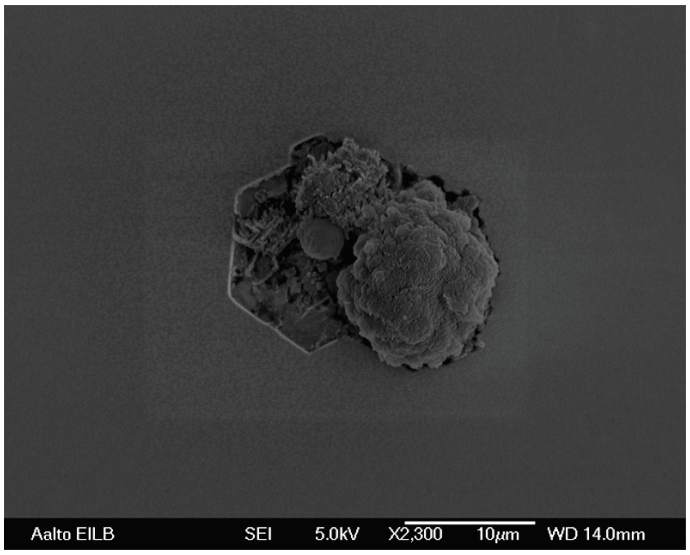

Figure 24: SEM micrograph of a particle on the AlN surface.

In order to test this hypothesis, the growth process was repeated using the same process parameters. This time the surface of the substrate was protected with a photoresist prior to dicing. The average particle density and size for both samples was determined using methods presented previously (Sec. 7.6) and are presented in Table 5. The p-values for the t-tests are presented as well.

Table 5: Average particle density and size for AlN samples 1 (without protection) and 2 (with protection), along with p-values for the t-tests.

Sample	Density (mm^{-2})	Size (μm)
1	1.20	11.55
2	0.71	9.39
p-value	0.0010	0.1384

According to the results, there was a statistically significant difference in the measured particle density of the two samples. This indicates that the observed AlN particles were caused by, at least partially, by dicing induced particles. However, completely particle free sample was not produced by the photoresist protection. This indicates that there are other possible sources of particles, or that the photoresist was not completely efficient in protecting the substrate surface from dicing particles. Other sources of particles include the aforementioned parasitic reactions and pre-deposits from the MOVPE reactor walls and showerhead.

The average particle size was smaller for the second sample, although the high p-value indicates that there was not a statistically significant difference in them. This indicates that the source of particles on both samples was the same. Representative particle densities and sizes are presented in Figures 25 and 26, respectively for both samples.

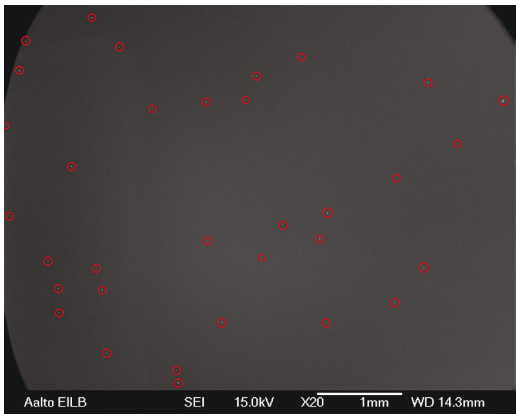

(a) Sample 1, particle density 1.21 mm^{-2}

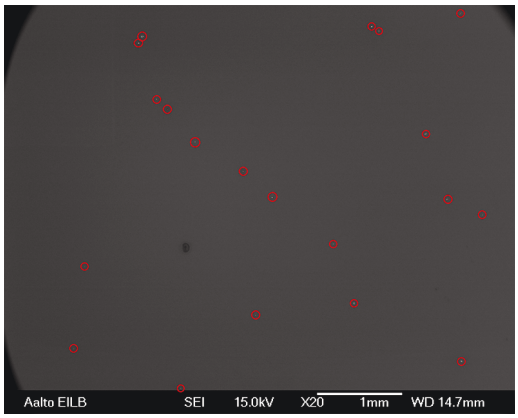

(b) Sample 2, particle density 0.74 mm^{-2}

Figure 25: SEM micrographs of both samples with particle densities closest to the average, observed particles highlighted with red circles.

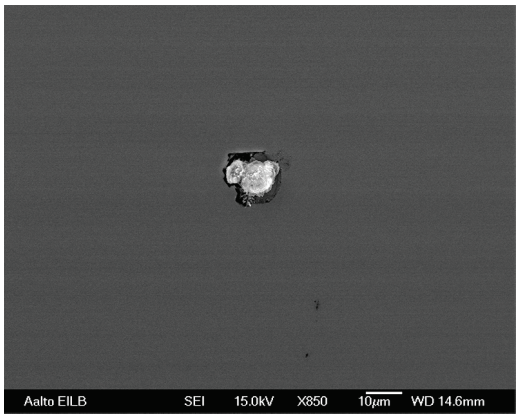

(a) Sample 1, particle diameter approximately 11.8 μm

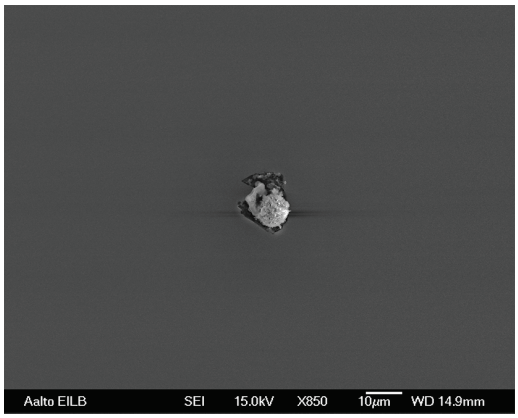

(b) Sample 2, particle diameter approximately 9.2 μm

Figure 26: Representative pictures of average particle size on both samples.

Some error in the results can be expected due to the method used, especially in the particle size. All particles were assumed to be spherical and the diameter was measured only along one randomly selected axis. Moreover, the selection method may have favoured larger particles over smaller ones, simply because the former were more noticeable. In the particle density measurement it is possible that the smallest of particles were not counted, resulting in a lower density value. However, even though the results may not represent the absolute values, they are comparable to each other.

In addition, the particles affected the AlN film around them, as can be seen in Figure 27. The effect was more pronounced for sample 1 (Fig. 28a) than for sample 2 (Fig. 28b). The lighter areas are significantly larger on sample 1 than on sample 2. Moreover, the contrast is starker on sample 1. The lighter areas seen in the pictures are probably aluminium rich phases.

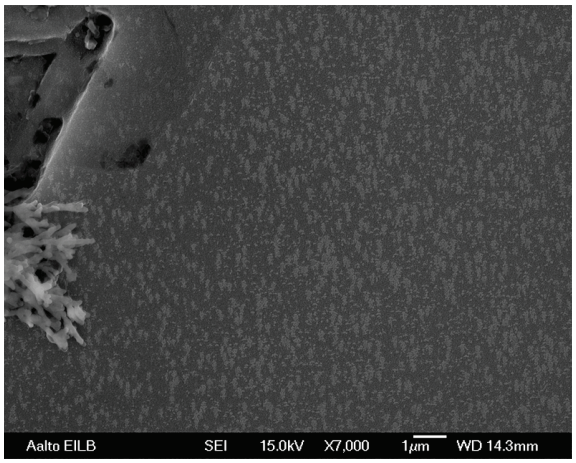

Figure 27: Surface of the AlN film near one of the particles.

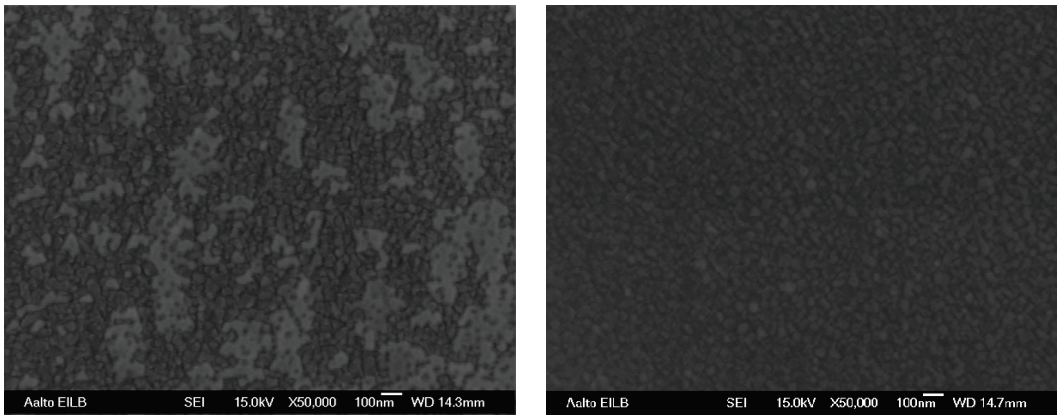

(a) Sample 1. (b) Sample 2.

Figure 28: Surface of the AlN film near a particle.

There is no noticeable difference between the sample surfaces away from the particles. The surface looks relatively smooth and uniform across the sample. However, the surface has a definite texture, as seen in Figure 29. This may indicate that the AlN film is polycrystalline in structure and the growth followed one of the island growth modes.

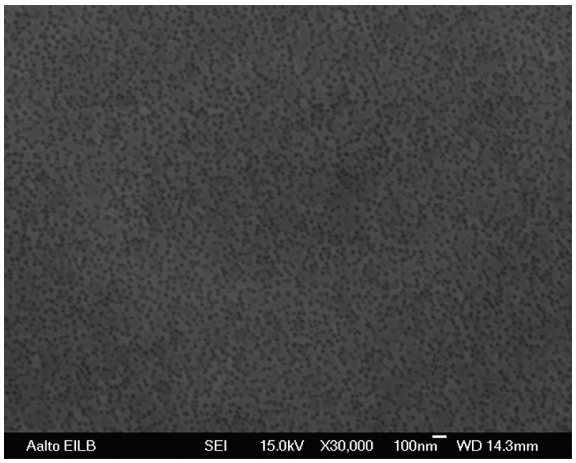

Figure 29: Surface of the AlN film.

In conclusion, the observed particles were at least partially caused by the dicing and not because the growth process itself. The large size of the particles may indicate that they are not only growth based. The film thickness itself was 83 nm, while the particles were significantly larger. One possible explanation that micrometre sized particles existed already on the substrate, and those were covered with AlN during the growth. Other possible source of the particles is the growth reactor itself. AlN and other particles from previous growth processes could have ended on the substrate as a result of insufficient reactor cleaning.

The surface of the film was relatively smooth and uniform everywhere else except near the particles. The texture of the surface may indicate polycrystalline structure. Moreover, the film may have grown in one of the island growth modes. Near the particles, sample 2 surface looked significantly better than sample 1. It is worth noting that particle reduction by photoresist protection during dicing is not an important part of this work. The previous analysis was however needed in order to rule out possible issues in the growth process.

8.4 Effect of Growth Time and Temperature

The growth time and temperature were varied in order to determine their effect mainly on the crystal quality, as previously presented in 7.4. Additionally, from these experiments the growth rate at a constant temperature was defined with more accuracy. The effect of the growth temperature on growth rate was studied as well. The results of growth time on film thickness and crystal quality are presented in Table 6 and the results of growth temperature on crystal quality and film thickness are presented in Table 7.

Table 6: Results of different growth times on film thickness and crystal quality.

Growth time (min)	Thickness (nm)	2θ-ω FWHM (°)	ω FWHM (°)
12.5	49	N/A	N/A
25	83	0.21	0.51
60	220	0.15	1.49
90	270	0.14	1.15
120	410	0.15	1.01
160	540	0.10	0.72

Table 7: Results of different growth temperatures on crystal quality and growth rate.

Temperature (°C)	2θ-ω FWHM (°)	ω FWHM (°)	Growth rate (nm/min)
1 125	0.21	0.51	3.32
1 000	0.31	2.68	3.54
875	-	-	3.51
750	-	-	3.57

The film thickness as a function of growth time is presented in Figure 30. The results clearly indicate that the thickness is linearly dependent on the growth time. The growth rate is approximately 3.34 nm/min. The constant term of the fitted line corresponds to the thickness of the low temperature AlN seed layer. The measurement error was assumed to be two times the standard deviation of the ellipsometry measurements.

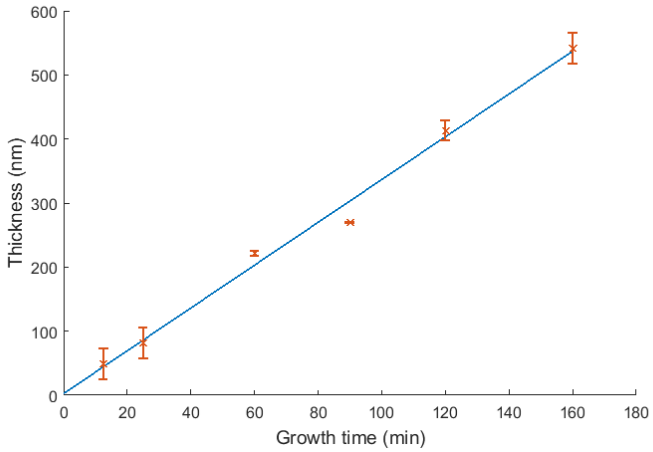

Figure 30: Film thickness as a function of growth time. A simple linear regression line is fitted in least squares sense in blue, with $R^2 = 0.9913$.

Compared to growth rates of sputtered AlN, growth rate of 3.34 nm/min is relatively low. With respect to MOVPE grown AlN results, this is a comparable growth rate. Rate of 5.6 nm/min has been reported for an AlN film with a ω scan

FWHM of 0.30° to 0.35° for a 300 nm thick film [36]. It was reported that the FWHM value decreased with increasing film thickness. Compared to this, the results achieved in this work are in good agreement. Other reported growth rates are up to 15 nm/min [53]. However, no analysis of the crystal quality of these films were done.

The measured 2θ-ω and ω scan peaks are presented in Figure 31. The intensity of the measured peaks increases as a function of the film thickness. This is simply because the scattering volume increases. There is no significant change in the crystal quality as a function of film thickness. The small decrease in 2θ-ω FWHM values is, at least in part, due to the increase in the signal-to-noise ratio.

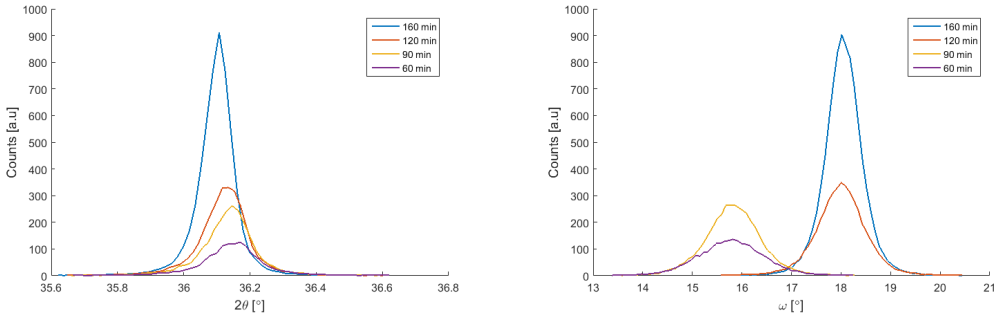

(a) 2θ-ω scans. (b) ω scans.

Figure 31: XRD measurements of 160, 120, 90 and 60 min growth times.

The preferred orientation of the c-axis seems to improve as the thickness increases, indicated by the decreasing ω FWHM. It has been suggested that this occurs because grains near the substrate boundary are not as oriented as those that grow on top of them. As the film thickness increases, the ratio between grains near the boundary and away from it simply changes, and the measured ω-peak becomes narrower. [21]

The location of the 2θ peak maximum shifts to lower values from 36.17° to 36.11°. This shift is not significant, however it is consistent in the results. This means that the measured lattice constant c changes from 4,963 Å to 4.971 Å. As the thickness increases, the lattice constant increases as well, approaching the unstrained value of $c_0 = 4.978 \cdots 4.981$ Å. Thus, with increasing thickness the film becomes increasingly relaxed through the generation of dislocations, as was expected.

The location of the ω-scan peak maxima show a peculiar change between 120 and 90 minute growth times. The source of the 2° shift between the peaks is unknown. It could be that for some reasons the grains of the two samples have a 2° tilt with respect to the surface normal. Other possibility is an instrumental error.

From a crystal quality point of view, the thicker films seem to give the best results. However, there is a limit to the thickness of the film. In the thickest film, fractures on the surface were observed, as seen in Figure 32. The cracks are most likely created by the stress caused by the CTE mismatch between the film and the substrate, which increases as the film thickness increases. Between 410 and 540 nm the stress is enough to cause cracks. The observer cracks seem to follow crystal planes at hexagonal angles. Otherwise the surface of the AlN film was similar to the results presented earlier in Section 8.3.

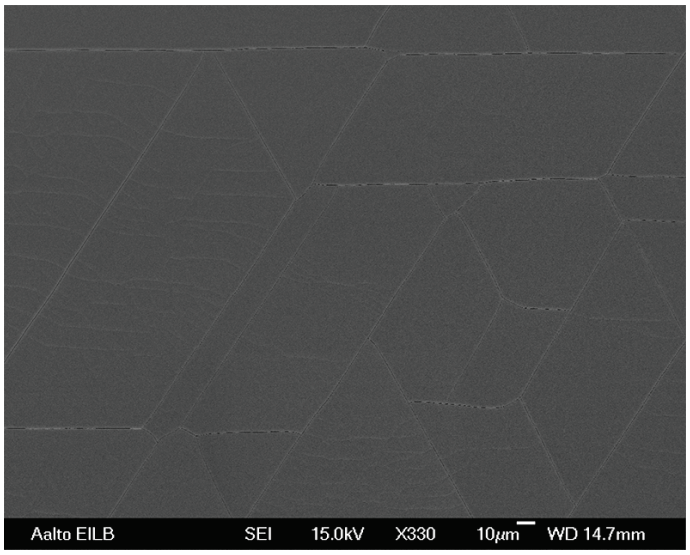

Figure 32: SEM micrograph of the 540 nm thick AlN film. Fractures are observed along the crystal planes.

In Figure 33 the growth rate is presented as a function of growth temperature. The results show that the growth rate increases with decreasing temperature. However, the change is not significant, especially in the range of $750 \cdots 1000$ °C. The decrease in growth rate is probably a result of the increased evaporation rate of the already grown AlN film. The evaporation can have a significant effect on the crystal quality. The high substrate temperature evaporates the most loosely bound atoms that are not in their correct lattice points. Moreover, evaporation of incorporated impurities could also occur.

The constant growth rate indicates that the AlN growth is transport limited. The reactions consume the precursors faster than they are supplied. The growth rate could be increased by increasing the flow rates of the precursors. While this would make the process faster, it might decrease the crystal quality.

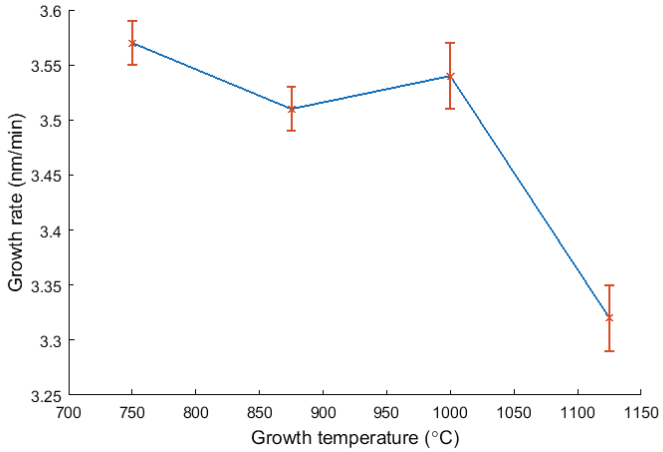

Figure 33: Growth rate as a function of growth temperature.

The crystal quality decreased significantly as the growth temperature was decreased. The 002 reflection was only faintly observed for the film grown at 1 000 °C using the closed detector, as shown in Figures 34a and 34b, for the 2θ-ω and ω scans, respectively. For the films grown at lower temperature, no 002 reflections were observed at all using the closed detector. Using the open detector, the peaks could be observed even for these films. However, the results are not comparable between closed and open detector measurements.

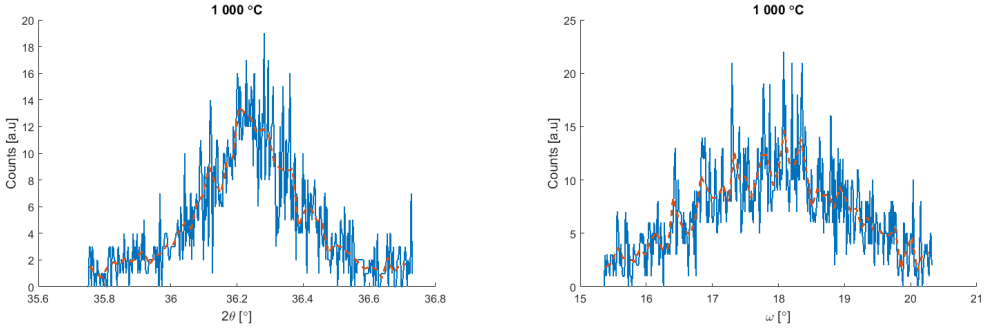

(a) 2θ-ω scan. (b) ω scan.

Figure 34: XRD measurements of sample grown at 1 000 °C.

In conclusion, the crystal quality of the AlN films grown at 1 125 °C should be sufficient for good piezoelectric properties. The growth temperature cannot be reduced without severe deterioration of the crystal quality. The thickness of the film does not affect the quality of the film as such. However, the maximum thickness of the film was determined to be approximately 500 nm before it cracks.

9 Conclusions

The purpose of this Master's Thesis was to identify suitable materials and methods for in-plane piezoelectric actuation for MEMS sensors. The main goal was the selection of the piezoelectric material and its growth method. The theory of piezoelectricity along with piezoelectric actuation and sensing, and different piezoelectric materials were presented in Section 2.

The selection of the piezoelectric material was discussed in more detail in 2.2. The material needed to fill certain requirements specific to this work in addition to what is generally required for piezoelectric materials. For example, strong piezoelectric effect and compatibility with commonly used materials and methods in MEMS devices is required. In addition, important aspects in the selection were availability and existing growth methods of the material. Dielectric constant and strength were a factors as well.

Different piezoelectric materials were considered, such as quartz, lead zirconate titanate, zinc oxide and aluminium nitride. Out of the different options, AlN was selected as the most suitable one. The piezoelectric effect of AlN is not the strongest of the materials available. The transverse constant d_{31} for AlN is just -2.0 pC/N, whereas PZT can have constants as high as -274 pC/N [3]. However, the other properties of AlN are well suited to this work compared to other materials. Mainly, it is compatible with other materials and methods, it can be grown with a wide range of methods and it is already widely used in the MEMS field. Moreover, it is suitable for sensing as well, because the dielectric constant is one of the smallest.

The piezoelectric properties of a material do not depend only on its bulk values. They are influenced by the crystal quality and orientation to a great extent as well. These in turn are defined by the material growth. Because of this, the growth of crystals and different growth methods were presented in Sections 3 and 4, respectively.

The AlN growth capability of each method was discussed along with typical crystal quality of films produced. Different PVD and CVD methods were considered, such as reactive sputtering (4.3) and MOVPE (4.4). This work required that the selected method is capable of growing piezoelectric AlN on vertical sidewalls. Usually, this does not need to be considered when selecting a growth method. In this work however, it was one of the main deciding factors and the second major focus of this thesis.

Out of all the considered methods, MOVPE was selected as the most suitable one for three main reasons. First, it has been previously used to grow AlN and the process is relatively well understood. Moreover, MOVPE grown thin films are typically of high crystal quality, enabling a strong piezoelectric response. Finally, the growth on vertical sidewalls should be good. Other compared methods cannot fulfil all the requirements needed in this work.

Because the surface properties upon which the piezoelectric material is grown affect its properties, the electrode and beam fabrication were discussed as well in Section 5. The electrode needs to promote the growth of high quality piezoelectric material. Moreover, the surface of the substrate, or in this case the vertical sidewall, needs to be adequately smooth and have the right crystal orientation. In addition,

the operating principle of gyroscopes and why in-plane actuation is needed was presented as well.

Molybdenum was selected out of the different materials considered as the electrode material. It has the smallest lattice mismatch with AlN (−1%) and its melting point (2 610 °C) is high enough the withstand typical AlN growth temperatures (> 1 000 °C) [13, 39]. One drawback of Mo is that it reacts with Si and requires a diffusion barrier. A thin layer of AlN could be used as the barrier. Another barrier layer option is thermal SiO_2.

For the fabrication of the actuator beam, a relatively simple process was suggested. It uses a (110) SOI substrate and combines reactive ion etching and anisotropic wet etching. This process should results in a well defined beam with smooth sidewalls in the correct crystallographic orientation.

In the experimental part of this thesis the characterization methods used were presented first in Section 6. Next in Section 7 the developed AlN growth process was presented. Other steps of the sample fabrication and conducted experiments were presented as well.

The performance of two different actuator configurations were compared using FEM simulation. The effect of piezoelectric material thickness on performance was simulated as well. The surface features and crystal quality was studied by analysing the AlN films grown with the developed MOVPE process. In addition, the effect of film thickness on crystal quality was measured as well. The effect of growth temperature on AlN crystal quality and growth rate was analysed as well.

The results were finally presented in Section 8. The FEM results showed that the proposed sidewall actuator configuration had increased performance compared to the split electrode one. The generated in-plane displacement using otherwise same actuator structure increased from 21 nm to 53 nm if the actuator structure was narrow. In other words, the actuation performance of the sidewall configuration was approximately 250% compared to the alternative. In the case of significantly wider structure, the in-plane displacement of the two configurations was approximately the same. However, the split actuator configuration suffered from unwanted twisting motion, whereas the sidewall actuator did not.

The results also showed that a thinner piezoelectric element is not better than a thicker one as such. However, the effect of the piezoelectric material on the elastic properties of the whole actuator structure needs to be considered. In general, thinner layers yield higher performance according to the simulation. Though the significance of the material thickness decreases as it becomes a smaller fraction of the total device width.

The crystal quality results indicated that the selected growth method and parameters were suitable for the growth of piezoelectric AlN. In fact, the crystal quality was better than most other reported results. The measured FWHM values that give indication of the quality were approximately 0.2°, whereas other reported values are in the range of 2°. Although all results are not directly comparable due to different growth and measurement methods.

The results also showed that the measured films were polycrystalline and had the desired orientation of the polar *c*-axis and that different grains were well oriented

in the same direction. Moreover, the measured values for the lattice constant c showed that the films were almost completely unstrained AlN. The measured values were approximately 4.97 Å, whereas the commonly reported values for the reference constant are in the range of 4.78 Å [9].

Micrometre sized particles and holes around them were observed on the AlN films. Elemental analysis of the particles showed that they were at least in part AlN. Particle generation is a known problem in MOVPE due to parasitic reactions. However, it was concluded this was not the source of the observed particles. Instead, they were most likely caused by pre-existing particles on the samples.

The measured crystal quality did not change significantly with respect to film thickness. The measured FWHM value decreased from 0.21° to 0.10° when the film thickness was increased from 83 nm to 540 nm. However, there is a limit to the maximum film thickness. Fractures were observed when the film thickness was 540 nm. Thus, the thickens of the piezoelectric film should not affect the performance of the actuator, as long as it does not exceed approximately 500 nm.

The growth temperature had a significant effect on the crystal quality. The results showed that the best growth temperature with respect to crystal quality was 1 125 °C. The 002 XRD reflection peak used in defining the crystal quality was only barely observable for the film grown at 1 000 °C and the preferential alignment of the polar c-axes decreased as well. For films grown at lower temperatures no peaks could be measured at all. Thus, the growth temperature cannot be decreased from 1 125 °C.

The results showed that the growth rate at 1 125 °C was 3.34 nm/min. This is relatively slow compared to other growth methods, for example sputtering growth rates of 15 nm/min [53]. The growth rate did not change significantly as a function of growth temperature. It increased from 3.32 nm/min to approximately 3.54 nm/min when temperature was decreased from 1 125 °C. This indicates that the growth of AlN was transport and not reaction limited. The rate could be thus increased by increasing the supply of TMAl.

In conclusion, the results of this Master's Thesis indicate that the selected material and growth method are suitable to be used in the realization of a high performance piezoelectric in-plane actuator. Small improvements to the MOVPE process could still be made.

9.1 Future Research

In this work AlN was only grown on horizontal surfaces. For future research, the first step should be the growth of AlN using the selected method on vertical surfaces. This should be done in order to confirm the conformal coverage of the method, which was not done in this work. As mentioned before, the conformal coverage of MOVPE and CVD methods in general should be adequate. However, this has not been experimentally confirmed. Additionally, the crystal structure of the grown films should be studied.

After this, attention to the electrode material and to its deposition method should be given. The electrode material was only suggested in this work and the deposition method was not in the scope of this thesis.

The deposition of the electrode material should be studied on vertical surfaces. It needs to meet the same requirements as for the AlN growth. Moreover, the crystallinity of the electrode is an important factor as well because it influences the crystallinity of AlN. The electrode crystallinity and growth on vertical surfaces should be similarly studied as AlN was studied.

Finally, once both the electrode and AlN have been separately studied their interaction needs to be characterized as well. All processes should be optimized by combining all the materials and methods into one process and then characterizing again the crystallinity and the conformal growth.

The piezoelectric performance should be characterized as well by measuring the piezoelectric coefficients. This can and should be done once the fabrication of electrode structures is possible.

References

[1] Ville Kaajakari. *Practical MEMS*. Small Gear Publishing, [Las Vegas, Nev.], 2009.

[2] Susan Trolier-McKinstry and Peter Muralt. Thin Film Piezoelectrics for MEMS. *Journal of Electroceramics*, 12(1-2):7–17, 2004.

[3] Robert E. Newnham. *Properties of Materials: Anisotropy, Symmetry, Structure*. Oxford University Press, Oxford, 2005.

[4] Marc-Alexandre Dubois and Paul Muralt. Properties of Aluminum Nitride Thin Films for Piezoelectric Transducers and Microwave Filter Applications. *Applied Physics Letters*, 74(20):3032–3034, 1999.

[5] J.J. Cupal. Dielectric, Piezoelectric, and Electromechanical Coupling Constants of Zinc Oxide Crystals. *Proceedings of the IEEE*, 56(2):225–226, Feb 1968.

[6] Isaku Kanno, Hidetoshi Kotera, and Kiyotaka Wasa. Measurement of Transverse Piezoelectric Properties of PZT Thin Films. *Sensors and Actuators A: Physical*, 107(1):68–74, 2003.

[7] R Bechmann. Elastic and Piezoelectric Constants of Alpha-quartz. *Physical review*, 110(5):1060, 1958.

[8] RoHS Directive. Directive 2002/95/ec of the european parliament and of the council of 27 january 2003 on the restriction of the use of certain hazardous substances in electrical and electronic equipment. *Official Journal of the European Union*, 13:L37, 2003.

[9] MA Moram and ME Vickers. X-Ray Diffraction of III-Nitrides. *Reports on Progress in Physics*, 72(3), 2009.

[10] Paul K. Chu. Novel Silicon-on-Insulator Structures for Reduced Self-Heating Effects. *Circuits and Systems Magazine, IEEE*, 5(4):18–29, 2005. ID: 1.

[11] Marian A. Herman, Wolfgang Richter, and Helmut Sitter. *Epitaxy: Physical Principles and Technical Implementation*. Springer, Berlin, 2004.

[12] Yoshitaka Taniyasu and Makoto Kasu. Improved Emission Efficiency of 210-nm Deep Ultraviolet Aluminum Nitride. *NTT Tech. Rev*, 8(1), 2010.

[13] Sami Franssila. *Introduction to Microfabrication*. John Wiley & Sons, Chichester, West Sussex, England, 2nd ed. edition, 2010.

[14] Pallab Bhattacharya. *Semiconductor Optoelectronic Devices*. Prentice-Hall, Inc., 1994.

[15] Jie-Fang Li, D. D. Viehland, T. Tani, C. D. E. Lakeman, and D. A. Payne. Piezoelectric Properties of Sol-Gel Derived Ferroelectric and Antiferroelectric Thin Layers. *Journal of Applied Physics*, 75(1):442–448, 1994.

[16] Ph Luginbuhl, G. . Racine, Ph Lerch, B. Romanowicz, K. G. Brooks, N. F. de Rooij, Ph Renaud, and N. Setter. Piezoelectric Cantilever Beams Actuated by PZT Sol-Gel Thin Film. *Sensors and Actuators A: Physical*, 54(1-3):530–535, 6 1996.

[17] Jeong Hwan Park, Fei Xu, and Susan Trolier-McKinstry. Dielectric and Piezoelectric Properties of Sol-gel Derived Lead Magnesium Niobium Titanate Films with Different Textures. *Journal of Applied Physics*, 89(1):568–574, 2001.

[18] M Kobayashi, T.R Olding, M Sayer, and C.-K Jen. Piezoelectric Thick Film Ultrasonic Transducers Fabricated by a Sol-Gel Spray Technique. *Ultrasonics*, 39(10):675 – 680, 2002.

[19] S. Yoshida, S. Misawa, and A. Itoh. Epitaxial Growth of Aluminum Nitride Films on Sapphire by Reactive Evaporation. *Applied Physics Letters*, 26(8):461–462, 1975.

[20] Xiangjun He, Si-Ze Yang, Kun Tao, and Yudian Fan. Materials Science Communication Formation of AlN Films by Al Evaporation with Nitrogen Ion Beam Bombardment. *Materials Chemistry and Physics*, 51(2):199–201, 11 1997.

[21] HP Loebl, C Metzmacher, RF Milsom, P Lok, F Van Straten, and A Tuinhout. RF Bulk Acoustic Wave Resonators and Filters. *Journal of Electroceramics*, 12(1-2):109–118, 2004.

[22] Fredrik Engelmark, G Fucntes, IV Katardjiev, A Harsta, Ulf Smith, and Sören Berg. Synthesis of Highly Oriented Piezoelectric AlN Films by Reactive Sputter Deposition. *Journal of Vacuum Science & Technology A*, 18(4):1609–1612, 2000.

[23] Xiao-Hong Xu, Hai-Shun Wu, Cong-Jie Zhang, and Zhi-Hao Jin. Morphological Properties of AlN Piezoelectric Thin Films Deposited by DC Reactive Magnetron Sputtering. *Thin Solid Films*, 388(1):62–67, 2001.

[24] M Ishihara, SJ Li, H Yumoto, K Akashi, and Y Ide. Control of Preferential Orientation of AlN Films Prepared by the Reactive Sputtering Method. *Thin Solid Films*, 316(1):152–157, 1998.

[25] Gonzalo Fuentes Iriarte, Fredrik Engelmark, and Ilia V Katardjiev. Reactive Sputter Deposition of Highly Oriented AlN Films at Room Temperature. *Journal of Materials Research*, 17(6):1469–1475, 2002.

[26] Hiroshi Okano, Yusuke Takahashi, Toshiharu Tanaka, Kenichi Shibata, and Shoichi Nakano. Preparation of c-Axis Oriented AlN Thin Films by Low-temperature Reactive Sputtering. *Japanese journal of applied physics*, 31(10R):3446, 1992.

[27] N Nepal, SB Qadri, JK Hite, NA Mahadik, MA Mastro, and CR Eddy Jr. Epitaxial Growth of AlN Films via Plasma-Assisted Atomic Layer Epitaxy. *Applied Physics Letters*, 103(8):082110, 2013.

[28] Marc-Alexandre Dubois and Paul Muralt. Stress and Piezoelectric Properties of Aluminum Nitride Thin Films Deposited onto Metal Electrodes by Pulsed Direct Current Reactive Sputtering. *Journal of Applied Physics*, 89(11):6389–6395, 2001.

[29] Morito Akiyama, Keigo Nagao, Naohiro Ueno, Hiroshi Tateyama, and Tetsuo Yamada. Influence of Metal Electrodes on Crystal Orientation of Aluminum Nitride Thin Films. *Vacuum*, 74(3-4):699–703, 6/7 2004.

[30] Roozbeh Tabrizian and Farrokh Ayazi. Sputter Deposition of Piezoelectric AlN Thin Films on Vertical Walls of Micromechanical Devices. In *Proceedings of the 2nd International Workshop on Piezoelectric MEMS*, 2011.

[31] Armin Dadgar. Sixteen Years GaN on Si. *physica status solidi (b)*, 252(5):1063–1068, 2015.

[32] M Kneissl, T Kolbe, C Chua, V Kueller, N Lobo, J Stellmach, A Knauer, H Rodriguez, S Einfeldt, Z Yang, et al. Advances in Group III-Nitride-Based Deep UV Light-Emitting Diode Technology. *Semiconductor Science and Technology*, 26(1):014036, 2011.

[33] Theodoros G. Mihopoulos, Vijay Gupta, and Klavs F. Jensen. A Reaction-Transport Model for AlGaN MOVPE Growth. *Journal of Crystal Growth*, 195(1-4):733–739, 12/15 1998.

[34] Wolfgang Richter and Dietrich Zahn. Analysis of Epitaxial Growth. In *Optical Characterization of Epitaxial Semiconductor Layers*, pages 12–67. Springer, 1996.

[35] AV Lobanova, KM Mazaev, RA Talalaev, M. Leys, S. Boeykens, K. Cheng, and S. Degroote. Effect of V/III Ratio in AlN and AlGaN MOVPE. *Journal of Crystal Growth*, 287(2):601–604, 2006.

[36] Armin Dadgar, A. Krost, J. Christen, B. Bastek, F. Bertram, A. Krtschil, T. Hempel, J. Blasing, U. Haboeck, and A. Hoffmann. MOVPE Growth of High-quality AlN. *Journal of Crystal Growth*, 297(2):306–310, 2006.

[37] Si-Hyung Lee, Jeon-Kook Lee, and Ki Hyun Yoon. Growth of Highly c-Axis Textured AlN Films on Mo Electrodes for Film Bulk Acoustic Wave Resonators. *Journal of Vacuum Science & Technology A*, 21(1):1–5, 2003.

[38] Karen Holloway, Peter M. Fryer, Cyril Cabral, J. M. E. Harper, P. J. Bailey, and K. H. Kelleher. Tantalum as a Diffusion Barrier Between Copper and Silicon: Failure Mechanism and Effect of Nitrogen Additions. *Journal of Applied Physics*, 71(11):5433–5444, 1992.

[39] Wheeler P. Davey. Precision Measurements of the Lattice Constants of Twelve Common Metals. *Physical Review*, 25:753–761, Jun 1925.

[40] R M Wood. The Lattice Constants of High Purity Alpha Titanium. *Proceedings of the Physical Society*, 80(3):783, 1962.

[41] Guoqiang Li, Tae-Won Kim, Shigeru Inoue, Koichiro Okamoto, and Hiroshi Fujioka. Epitaxial Growth of Single-crystalline AlN Films on Tungsten Substrates. *Applied Physics Letters*, 89(24), 2006.

[42] C-M Yang, K. Uehara, S-K Kim, S. Kameda, H. Nakase, and K. Tsubouchi. Highly c-Axis-Oriented AlN Film Using MOCVD for 5GHz-band FBAR Filter. In *Ultrasonics, 2003 IEEE Symposium on*, volume 1, pages 170–173. IEEE, 2003.

[43] Raj Jakkaraju, G. Henn, C. Shearer, M. Harris, N. Rimmer, and P. Rich. Integrated Approach to Electrode and AlN Depositions for Bulk Acoustic Wave (BAW) Devices. *Microelectronic Engineering*, 70(2-4):566–570, 11 2003.

[44] Kirt R Williams, Kishan Gupta, and Matthew Wasilik. Etch Rates for Micromachining Processing - Part II. *Microelectromechanical Systems, Journal of*, 12(6):761–778, 2003.

[45] A. Guivarc'h, P. Auvray, L. Berthou, M. Le Cun, J. P. Boulet, P. Henoc, G. Pelous, and A. Martinez. Reaction Kinetics of Molybdenum Thin Films on Silicon (111) Surface. *Journal of Applied Physics*, 49(1):233–237, 1978.

[46] L. D. Locker and C. D. Capio. Reaction Kinetics of Tungsten Thin Films on Silicon (100) Surfaces. *Journal of Applied Physics*, 44(10):4366–4369, 1973.

[47] Harald Ibach and Hans Luth. *Solid-state Physics: an Introduction to Principles of Materials Science*. Advanced texts in physics. Springer, New York, 4th extensively up-dated and enl. ed. edition, 2009.

[48] Ray Egerton. *Physical Principles of Electron Microscopy: an Introduction to TEM, SEM, and AEM*. Springer Science & Business Media, 2006.

[49] Comsol multiphysics modeling software 5.1.

[50] Rajan S Naik, Joseph J Lutsky, Rafael Reif, Charles G Sodini, Andy Becker, Linus Fetter, Harold Huggins, Ronald Miller, John Pastalan, Gee Rittenhouse, et al. Measurements of the Bulk, c-Axis Electromechanical Coupling Constant as a Function of AlN Film Quality. *Ultrasonics, Ferroelectrics, and Frequency Control, IEEE Transactions on*, 47(1):292–296, 2000.

[51] Johan Bjurstrom, Daniel. Rosen, Ilia. Katardjiev, Ventsislav M. Yanchev, and Ivan Petrov. Dependence of the Electromechanical Coupling on the Degree of Orientation of c-Textured Thin AlN Films. *Ultrasonics, Ferroelectrics, and Frequency Control, IEEE Transactions on*, 51(10):1347–1353, Oct 2004.

[52] Gary S May and Costas J Spanos. *Fundamentals of Semiconductor Manufacturing and Process Control*. John Wiley & Sons, 2006.

[53] DG Zhao, JJ Zhu, DS Jiang, Hui Yang, JW Liang, XY Li, and HM Gong. Parasitic Reaction and its Effect on the Growth Rate of AlN by Metalorganic Chemical Vapor Deposition. *Journal of Crystal Growth*, 289(1):72–75, 2006.

A Simulation Parameters

In this appendix, the relevant material parameters used in the simulations presented in Section 7.1 are presented. The parameters are listed below in Table A1. The elasticity and piezoelectricity matrices are presented in full below.

Table A1: Material parameters used in the FEM simulations.

Parameter	AlN	Si
Density (kg/m^3)	3 300	2 329
Permittivity (ε_{ee})	10.2	11.7
Elasticity (GPa)	C_{AlN} (A1)	C_{Si} (A2)
Piezoelectricity (C/m^2)	e_{AlN} (A3)	0

$$\left(C_{AlN}\right) = \begin{pmatrix} 410 & 149 & 99 & 0 & 0 & 0 \\ 149 & 410 & 149 & 0 & 0 & 0 \\ 99 & 149 & 389 & 0 & 0 & 0 \\ 0 & 0 & 0 & 125 & 0 & 0 \\ 0 & 0 & 0 & 0 & 125 & 0 \\ 0 & 0 & 0 & 0 & 0 & 125 \end{pmatrix} \text{ GPa} \tag{A1}$$

$$\left(C_{Si}\right) = \begin{pmatrix} 166 & 64 & 64 & 0 & 0 & 0 \\ 64 & 166 & 64 & 0 & 0 & 0 \\ 64 & 64 & 166 & 0 & 0 & 0 \\ 0 & 0 & 0 & 80 & 0 & 0 \\ 0 & 0 & 0 & 0 & 80 & 0 \\ 0 & 0 & 0 & 0 & 0 & 80 \end{pmatrix} \text{ GPa} \tag{A2}$$

$$\left(e_{AlN}\right) = \begin{pmatrix} 0 & 0 & 0 & 0 & -0.48 & 0 \\ 0 & 0 & 0 & -0.48 & 0 & 0 \\ -1.02 & -1.02 & 1.55 & 0 & 0 & 0 \end{pmatrix} \text{ C/m}^2 \tag{A3}$$